Coupled Circuit Analysis of Eddy Currents in MRI Systems

Md. Shahadat Hossain Akram
Doctoral Program in Applied Physics

Submitted to the Graduate School of
Pure and Applied Sciences
in Partial Fulfillment of the Requirements
for the Degree of Doctor of Philosophy in
Engineering

at the
University of Tsukuba

Contents

Abstract

In this study, we performed coupled circuit numerical simulation of eddy currents in magnetic resonance imaging (MRI) systems by implementing novel approaches in subdomain modeling, inductive coupling calculations and in solving the system of coupled differential equations. Simulations were conducted for both open (0.3 T) MRI and closed-bore (9.4 T) superconducting MRI systems. In MRI systems, complex spatio-temporal eddy currents are induced in the surrounding conducting structures because of the switching of pulses in the gradient coils which is proportional to the inductive couplings among the gradient coils and different conducting structures and, decays with some characteristic time constants. In this study, following the dc resistive-inductive circuit concepts and the concepts of diffusion of eddy currents inside the materials with some characteristic skin depths, we divide the eddy current conducting structures into thin (much thinner than the skin depth) subdomains both along the length (or width) and thickness, and by implementing inductive coupling relations (of this network of coupled resistive-inductive circuits) we simulated the transient responses of eddy currents for subdomains at different locations of the conducting structures. We implemented the Eigen matrix method to solve the network of first-order coupled differential equations. To compute the coupling relations between the gradient coil and subdomains located at any position of the conducting structure, we implemented solid angle form of Ampere's law. The corresponding solid angles in three dimensions were calculated for both planar and cylindrical type of transverse (X- or Y-gradient) and longitudinal (Z-gradient) gradient coils. The secondary magnetic fields generated by the eddy currents were also calculated. Free induction decay (FID) experiments of eddy fields were conducted by using a nuclear magnetic resonance (NMR) probe to verify our simulation results for 0.3 T system and gradient echo shift technique was implemented for 9.4 T MRI system. We have found good agreements between simulation and experimental results.

Acknowledgements

Like many philosophical truths of life it is also true and we all have to admit that nothing is one's only credited contribution. This is how we get connected to others from various sectors of life and sometimes some connections last for the whole life and contribute for the improvement of earthly life. Likewise my PhD thesis – one of very important and valuable stages of my learning-life – is not my only-credited performance and, likewise I got connected to some excellent persons here in Japan through my PhD study starting from my very dear supervisor Katsumi Kose, PhD, Sensei to classmates, juniors, seniors, office staffs to whom I want to share the credits of my PhD study and successes. I would like to thank them all from the core of my heart. Few of those contributions and connections are worth mentioning here.

At first I would like to express my utmost gratitude and thankfulness to my supervisor Professor Katsumi Kose, PhD. His all-time smiling and appreciating guidance has been a great inspiration for me. It is a very refreshing research environment all the time in the NMR Imaging Laboratory of University of Tsukuba. He will remain as the best example for me to do research and to be a very kind supervisor at the same time. I would like to thank Yasuhiko Terada, PhD Sensei for his friendly guidance, valuable time, sincere concentration and many practical discussions and suggestions. I am very much grateful to my year-mate of my Laboratory Daiki Tamada, PhD – a very good research-centered person. I took many helps, suggestions from him and he has been a very good friend for me and will remain so. I am very much thankful to my PhD reviewers and two unknown journal paper reviewers. Many of their suggestions helped me much in planning differently and rightful way for different important research matters.

I am especially thankful to my wife Israt Jahan. It was really refreshing to go out for short tour - all of which she planned and managed. Many times I discussed my research works and improvements to her just for sharing and she listened carefully though many topics she might not understand clearly. Very especial thanks to my mother – for some people struggle of life are very different. I have learnt patience from her though still she is the coolest one even with her very weak heath condition and all-time struggling life. Thank you very much to my dear brother Md. Atiqur Rahman Ahad – a very exceptional human being and my all-time inspiration. Thanks to my large family members – three elder brothers and their wives and children, one younger sister, her husband and one new member to say 'hello' soon. Their regular communications did not let me feel homesickness. Close friends in Bangladesh – Mehdi, Rajib, Shopan, Rana and little friend Abid – thank you for your friendships. Especial thanks to Bangladeshi community in Tsukuba, Japan. Their many refreshing get-togethers, invitations, friendly communications and supports were exceptional and unexpected in abroad. It has been a very memorable time to study in University of Tsukuba, Japan. All praise be upon the almighty Allah.

Chapter 1

Introduction

1.1 MRI System: Basic in Brief

MRI is a non-invasive technique of imaging the internal physical and chemical characteristics of an object by employing radio frequency (RF) radiation in the presence of carefully controlled inhomogeneous static magnetic fields. Over the last 35 years, because of its excellent soft-tissue contrast and spatial resolution, MRI has progressed to a primary imaging technique in many sectors of clinical investigations that encompasses from neurological, cardiovascular examination to musculoskeletal examination. Because of its sensitivity to different physiological and biological parameters of the imaging object, like, flow, chemical composition and molecular configuration, it is well suited for functional and metabolic investigations. Recently it has become a clinical tool in conjunction with other modality of imaging techniques, like positron emission tomography (PET)/MRI, MRI-guided linear accelerator (LINAC) radiotherapy. The simultaneous PET/MRI has made it possible to investigate the functional and anatomical information of the object under examination and maximize the diagnostic certainty.

To generate images with high spatial resolution and excellent contrast without radiation-related hazard, MR imaging involves three kinds of non-ionizing fields, namely, a strong static magnetic field (B_o), a radio frequency (RF) field (B_1) and three magnetic field gradients along three Cartesian coordinate axes (namely, X-gradient coil (Gx), Y-gradient coil (Gy) and Z-gradient coil (Gz)). The imaging object is placed inside a strong homogeneous (i.e., 0.5 parts per million (ppm)) static magnetic field (B_o) that causes the magnetic moment vectors of nuclei of

different atoms, including hydrogen atom, to align with the direction (along Z-axis) of this external magnetic field - the nuclei of hydrogen atom are of particular interest in MR imaging [1]. The spin of hydrogen atom is called a spin-1/2 system in which the magnetic moment vectors possess one of two following orientations: (a) vectors pointing to the direction of B_o field (also called parallel), and (b) pointing to the opposite direction of the B_o field (antiparallel). At thermal equilibrium without external field these spins have random orientations that results in net zero magnetic moment in the macroscopic sense. But within an external field the population distribution in the parallel and antiparallel spin systems (ensemble of spins) show a very small of excess spin distribution in the lower energy states (parallel to the B_o field) as the spin is more likely to stay in the lower-energy state. In a bulk of atoms (called voxel in MR terminology – a three dimensional small volume (i.e., 1 mm × 1 mm × 1mm) of the object under investigation) these excess spin population distribution shows an observable macroscopic magnetization vector pointing along the direction of the B_o field which is called as bulk magnetization. If the external field is perfectly homogeneous the bulk magnetization vector rotates about the Z-axis with single precession/resonance frequency – an angular rotation that resembles the rotation of a top [2]. This rotational frequency is well known as Larmor frequency which is proportional to the externally applied B_o field. The proportionality constant is known as gyromagnetic ratio, γ – for the nuclei of hydrogen in an object the Larmor frequency is 42.58 MHz if applied B_o field is 1 T.

An RF field (B_1) with the frequency equal to the Larmor frequency is applied (by an RF transmit coil) perpendicular or transverse to the direction of the static field (B_o). B_1 is a circularly polarized transverse (X-Y plane) magnetic field that is applied to resonate with the precession frequency of the spin system in a voxel of the object under investigation. RF field is very short lived – few microseconds to milliseconds. After the resonance with the B_1 field, the spin systems

in the voxels absorb energy from the B_1 field and radiate the absorbed energy with the same Larmor frequency (which is received by the same or different RF coil). This signal is the primary interest for the MR imaging examination which is called the nuclear magnetic resonance (NMR) signal. But under large volume (i.e., a 5 mm thick transverse slice in a 40 cm diameter spherical volume) of homogeneous static magnetic field (B_o), these NMR signals from many small voxels of the object under investigation generate the similar NMR signals with characteristic Larmor frequency. To spatially encode these NMR signals of all voxels a third kind of low frequency switching magnetic field gradient is applied along the three Cartesian coordinate axes. These fields are known as gradient fields the Z-component of which generate a linear variation (controlled inhomogeneity) in the static magnetic field (B_o) along the three coordinate axes in the region of interest (ROI). The NMR signal in each voxel is now slightly different from the others. The received NMR signal in the RF receiver coil is the superposition of all these NMR signals from all of the voxels that contains in it the spatial information of the scanned region (this is also called as spatial encoding of the NMR signals). This spatial information from the complex NMR signal are decoded through Fourier transform and, by using image processing algorithms images are reconstructed, thereby calling it the magnetic resonance (MR) image.

1.2 Generation of Eddy Currents in MRI System

In MRI system time dependent gradient pulse with fast switching is required to apply in the gradient coils that generates targeted spatial variation of the static magnetic fields within the imaging volume and spatially encode the nuclear magnetic resonance (NMR) signals in three dimensions (3D) to generate images within reasonable time and accuracy. The combination of different gradient pulses and RF pulses needed to generate MR images is called MR sequence. A simple one dimensional imaging sequence is shown in Fig. 1.1 (a), and the projected imaging

area selected by this sequence is shown in Fig 1.1 (b) [1]. From this simple sequence we see that many gradient pulses are needed in MR imaging which are generated by using three different gradient coils. In general these gradient pulses are of trapezoidal shape with short rising (ramp-up) and falling (ramp-down) durations and a constant amplitude flat-top portion as is illustrated in Fig. 1.2. During the rising and falling portions of the gradient pulses in the gradient coils time-dependent magnetic fields are generated in the surrounding space. According to Faraday's law of electric induction [3] these changing magnetic fields induce electric field in space and if there is closed conducting structure within this electric field eddy currents are generated with complex temporal and spatial response characteristics. According to Lenz's law [3] the induced eddy currents opposes the changes in the switching current in the gradient coil and generates different adverse effects in the MRI system and images.

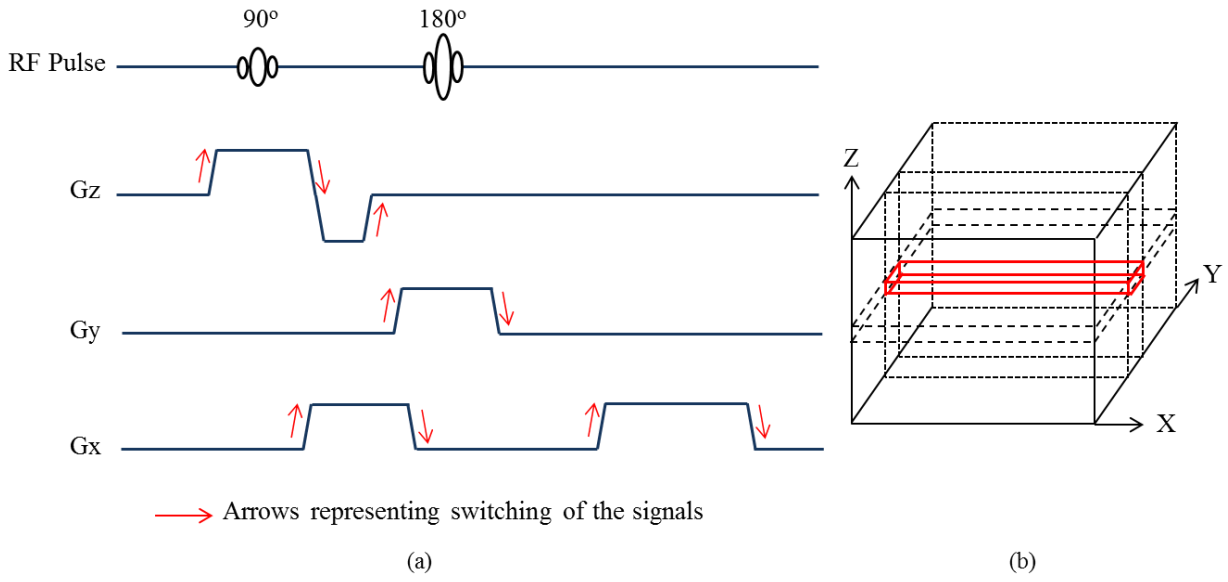

Fig. 1.1. (a) A simple MR sequence for 1-dimensional imaging – red arrows are marking the switching of gradient pulses that are the reason for generating eddy currents in the MRI conducting structures. (b) the red solid line block is the region that can be selected by the MR sequences given in (a).

1.3 Effects of Eddy Currents on MRI System and Images

The switching of pulses in the gradient coil induces eddy currents in different metallic structures of the MRI systems. These eddy currents create adverse effects in the MRI systems in the form of Ohmic heating that changes the temperature of the magnetic circuits from the desired

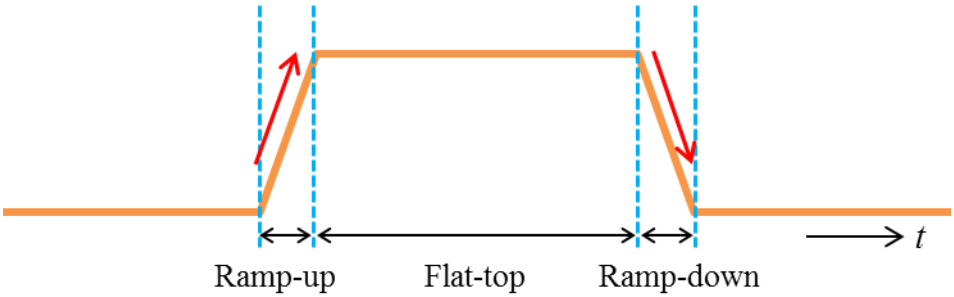

Fig. 1.2. An ideal trapezoidal shape signal showing

state and changes the operating temperature of the magnet which in turn can boil-up the cryostat materials – in extreme case magnet quenching might happen [4-5]; or, in the form of Lorentz force between conductors that in turn creates vibrations of the gradient assembly and other parts of the MRI system, radiates acoustic noise that hampers patient comfort and image quality [6,7], and sometimes creates oscillatory eddy currents in the system [2,8]; or, in the form of delays in the gradient-pulse switching (Lenz's law) that distorts the pulse shape and limits the application of faster imaging MR sequences [2,7]. Also eddy current generated time-varying secondary magnetic fields have adverse effects in the imaging region that causes spatial and temporal degradation of the applied linear primary gradient fields along the 3-dimensions (3-D) and distort the targeted spatial encoding of the NMR signals that resulted in misregistration of the NMR signals in the final image [8-11]. Different kinds of geometric distortions are generated in the images, like, shearing induced by read direction eddy current gradient, stretching induced by a phase direction eddy current gradient or shift of the images induced by a $B_o(t)$ eddy current field [5,11-13]. Geometric distortions become severe for diffusion imaging or echo planar imaging

(EPI) [13]. It also generates intensity-phase variation in both images and spectra [9]. On the other hand, with the advent of hybrid systems, like PET/MRI or MRI-guided radiotherapy, the accurate control of more complex eddy currents has become a critical topic in the research area [14]. To reduce these adverse effects both in the magnetic circuits and in the images, proper characterizations of both the eddy current responses and its secondary unwanted effects are a prime need in MRI research and development sectors.

1.4 Characterization of Eddy Currents in MRI Systems: Literature Review

Different measurement [12-21], and numerical calculation [4,6,9-10,22-37] approaches have been done in numerous literatures to characterize the eddy current responses in MRI systems considering the system structures, imaging objects and imaging methods.

1.4.1 Eddy Current Characterization by Measurement

Eddy current measurement methods can be mainly classified into two categories: free induction decay (FID) measurement of the NMR signals and phase/field mapping methods by implementing different MR sequences.

1.4.1.1 Free induction decay (FID) measurement method

In case of FID measurement, there have two techniques that are used according to the convenience or choice of the operators: single-phantom technique and multiple-phantom technique. In both cases a very small (i.e., few millimeter diameter spherical) phantom – sometimes called point-like phantom – within a small RF coil is placed at a precise position within the imaging region to measure the FID of the NMR signal of the phantom. To measure the effect of phase changes in the FID signal, a long duration gradient pulse is applied in the gradient system to generate eddy currents in the system. In case of single-phantom technique, a point-like phantom is placed at several positions within the imaging region and time evolution of FIDs of

NMR signals are measured after 90^o non-selective RF pulse and this process is repeated several times to acquire accurate data at multiple positions and delay times [2,8,12,16-17]. As a result, a full set of data acquisition with high accuracy becomes tedious for single phantom experiments. In the multiple-point-like-phantom technique there is no requirement of repositioning of the phantom and high temporal resolution is possible [12]. In [20-21] the point-like phantom technique is implemented by employing pure phase encode FIDs to monitor the arbitrary gradient waveform performances. This pure phase encode method is sensitive to low amplitude gradients (0.001) – 1 G/cm) and also can be possible to perform measurement of high amplitude gradients (10 – 300G/cm).

1.4.1.2 Phase Mapping Method

On the other hand, the phase mapping method does not necessarily require point-like phantom – large phantom can be used and eddy current phases are measured by using MR sequences of various kinds in accordance to the operator's requirements and/or MR application areas – like, echo planar imaging or radial imaging and so on. The data found from these experiments are exponentially fitted to multiple amplitudes and time constants as eddy currents responses are mostly assumed and proved to show multiexponential decaying characteristics [2,8,16-17]. Eddy current phase mapping by using stimulated echo (STEAM) imaging sequence is used in [18] to measure the phase along the 1-D projection of a large phantom. By using this process, results for both gradient eddy field and $B_o(t)$ eddy field can be calculated with one set of measurement. On the other hand, a rather easier gradient echo sequence is implemented in [19] – which can be called as gradient echo shift measurement method. Because of eddy current generated phase accumulation in the imaging region, the gradient echo is shifted from its intended position which can be measured and calculated to find the eddy current field responses.

In all of these cases, a reference scan is taken with no gradient signal to subtract the phases generated by other sources in the system.

1.4.2 Eddy Current Characterization: Analytical Calculation Approach

In the case of calculation, analytic expressions with simple geometries as flat plates, loops or sphere, and harmonic time-variations [38-39] are possible with Fourier integrals of modified Bessel functions by assuming the infinite length of the conducting structures. For finite length and complex geometries of the gradient coils and MR magnet structures, numerical analysis is required.

1.4.3 Eddy Current Characterization: Numerical Calculation Approach

Large-scale computational frameworks for the analysis of eddy current transient and spatial characteristics considering realistic cryostat conductors of intricate geometries in three dimensions has been developed extensively [24-37] by using finite element method (FEM) and finite-difference time-domain (FDTD) method at the expense of time consuming large computational loads and difficulties in defining the finite boundaries of the unbounded fields. Few important research works are summarized in this section.

The finite-element method is a numerical technique for finding approximate solutions to partial differential equations generated from problem under analysis which can be considered as boundary value problems. According to the FEM method, the region under investigation is divided into small subregions called finite-elements and, the problem equations are formed and solved for each small element considering the properties (material or electromagnetic properties, for example) of that particular element. The FEM method has proven to be an effective method for the analysis of field problems in electromagnetic engineering [40-45]. There are numerous research works that has also been done for numerical solution of eddy currents in MRI system by

using FEM method. M. Schinnerl et al implemented an FEM approach [24] for coupled magnetomechanical systems and developed an efficient calculation scheme that allows the analysis of three-dimensional (3-D) dynamic rigid motion as well as deformations of nonmagnetic and ferromagnetic materials in magnetic field. They modeled the 3-D mechanical problem related to eddy current generated vibrations in between the conducting structures of the superconducting magnet as discrete nodal elements, whereas the 3-D magnetic problem was modeled independently with edge elements. An FEM based magnetomechanical calculation scheme is also presented in [25] which was used to analyze the dynamical behavior of a clinical MRI system that include the optimization of the superconducting magnet considering eddy currents and vibrations in its cryostat. A finite element based multigrid algorithm with edge elements is explained in [26] for the calculation of transient 3-D eddy currents. To solve the large scale 3-D problems with reduced computational time a multiplicative Schwarz algorithm and a special Gauss Seidal iteration algorithm are compared in this study. Also, to find the repeated solution of eddy currents with different values of parameters, like frequency, permeability and conductivity, an efficient modeling and computational scheme is suggested in [27]. To avoid repeated solution of the entire FE model (thereby reducing the computational time) this algorithm updates the solution for different values of parameters by using a rather smaller sparse linear system. In this study [27], the transient responses of eddy current are computed as a superposition of responses of a number of harmonics. On the other hand, the high order frequency sensitivity of the time harmonic finite element formulation is implemented along with Fourier transform technique [28] in which the Fourier integral of continuous frequency is taken as Fourier series of discrete frequencies. The conversion of input waveform into discrete sinusoids and superposing their individual responses to generate the total response of the system

was made possible for a broad band of input waveform by implementing the high-order frequency sensitivity FEM method. In large scale scenario like eddy currents complex magnetomechanical problems in MRI magnets, these FEM calculations generate very large computational burden in generating and/or solving the system equations.

The finite-difference time-domain (FDTD) method is also another popular numerical electromagnetic calculation scheme for eddy current simulation in MRI system that discretizes the volume of space into small grids and solves the Maxwell's curl equations for an instant of time. The results of this instant is stored in the system and used to find results for the next step of time-instant and in this way the total time-space response is calculated step-wise for the system under consideration. But this method also suffers from large scale computational burden and boundary problems [32-37]. An efficient 3-D cylindrical FDTD method has been proposed by A. Trakic et al for the characterization of eddy current transient responses [32]. In this study the weakly coupled Maxwell's equations are modified for low-frequency region (as the eddy currents are induced by the low frequency switching of the gradient pulses) by downscaling the speed of the light constant by increasing either the permittivity or permeability of free space, but not both at the same time. This downscaling allows the use of larger FDTD time-steps and hence can reduce the computational loads. Still on a dual 3-GHz/4-Gb RAM workstation, it took 26 hours to compute the transient eddy current problem in 1cm thick/0.65-m-long conducting stainless steel cylindrical cryostat (300 K) and aluminum radiation shield (80 K) for both symmetric and asymmetric studies. To analyze the exponential decay of the eddy currents, exponential coefficients for the FDTD time-stepping are implemented in this study rather than using linear coefficients. To simulate the infinite unbounded computational domain an artificial boundary is introduced in the analysis that can result in errors which is resolved in this study by

introducing a perfectly matched layer (PML) in 3-D cylindrical coordinates as absorbing boundary conditions (ABC). This proposed method has been extended to optimize longitudinal gradient coil [9] in the presence of transient eddy currents by including the total-field scattered-field (TFSF) boundaries [33-34] that mimic the gradient coil and act as near field source. The temporal behavior of the gradient coil induced fields (i.e., pre-emphasized gradient excitation) are introduced by the TFSF technique. The advantages of implementing TFSF boundaries in the FDTD method is that the conductor and the small region of air neighboring the conductor are needed to be considered for the discretization into FDTD grids that reduces the computational time to several factors. A graphics process unit (GPU) based FDTD parallel-computing framework has been explained in [35] to overcome the limited computing performances of conventional CPU-based FDTD methods. This calculation approach also has the potential to calculate both detailed forward modeling and inverse design of MRI coils, which were previously impractical with FDTD method.

These conventional methods, such as the FDTD method or FEM method, have a time-consuming large-scale computational burden that requires very large memory and a high-performance computer—sometimes with parallel processing environments [32,36–37]. In addition, because of the large-scale computational complexity that combines the differential and integral techniques, there is a possibility of having numerical artifacts in the final results, like the artifacts because of interpolation in the transformation from lower dimensional grids to higher dimensional grids or field leakage across the boundary because of the slower propagation in the FDTD grid which differs from the propagation speed in the continuous world and so on [34].

Coupled circuit eddy current analysis method for MRI system [4,7,10,22-23,46-48] is an efficient and simple numerical calculation approach with the advantages of simple numerical

modeling features, less computational complexity and generating solutions comparable to the analytic eddy current calculations. The coupled circuit approach implements the advantages of differential equation and, matrix techniques to solve this system of first order differential equations that make it mathematically less complex and faster numerical simulation scheme. Following the coupled circuit method [22], eddy current conducting structures are modeled as inductively coupled subdomains and simple coupled differential equations are solved to find the transient responses of eddy currents in different subdomains.

Studies [7,22–23] using the coupled circuit approach were done on closed-bore (superconducting magnet) MRI systems and the coupled subdomains assumed for the cylindrical cryogenic walls were of circular ring-shaped. Simple inductive coupling formulas for computing the coupling relations between the subdomain and the gradient coils could be implemented in those studies. Also those studies concentrated on the model designing considering the Z-gradient induced eddy currents only. In references [4,47], a coupled circuit (named as network method) simulation - coupled in Fourier space - has been proposed for gradient coils of arbitrary geometry in cylindrical coordinates and validated by simulating the eddy current response in a finite length cylindrical cryostat induced by an actively shielded cylindrical X-gradient coil. This approach computes the eddy current responses for the discrete time steps of the applied gradient pulses that suffer from the possible oscillations of the Crank Nicholson method [49]. Also the X-gradient coil (of 18 turn per quarter) was discretized into 8000 wire segments and the whole simulation considering eddy current induced in the inner three bores took 25 minutes – though the author did not mention the computer resources they used for this simulation. A Multilayer Integral Method (MIM) [10] has been suggested in which the gradient coil conductors and eddy current conducting surfaces are approximated to a connected set of discrete mesh of plane

triangles – the number of triangles considered in this study for the eddy currents induced by one circular loop of Z-gradient coil in a 2.5 mm thick cylindrical conductor (with inner radius of 175 mm and length of 387 mm) was 27000. For 34 turn of Z-gradient coil it took almost 15 minutes to simulate the eddy current responses in one cylindrical bore. In all these studies there were no clear suggestions on how much thin should the sublayers be compared to the skin depth of the corresponding signal frequency – though it is suggested that sublayers thickness should be much smaller than the skin depth. Ideally, it should be infinitely thin. It has been suggested in [47] that the thickness should be less than one-fifth of the skin depth, whereas in reference [48] the thickness considered was less than one-third of the skin depth.

1.5 Purpose of this Study

The purpose of this study is to perform coupled circuit simulation of eddy currents for both open MRI (planar type gradient coil) and closed bore MRI (cylindrical type gradient coil) systems by implementing simple modeling and calculation approaches that would be easy to understand, would reduce the computational time and complexity, and easier to implement for any types of gradient coil configurations and any geometry of eddy current conducting structures. In this study we performed simulation for a 0.3 T open MRI system dedicated for child growth rate measurement [51] and a 9.4 T closed narrow-bore (54 mm dia.) MRI system dedicated for MR microscopic study. Simulations were conducted considering both the longitudinal (Z-) gradient and transverse (X- or Y-) gradient coil's induced eddy currents in linear conductors for both MRI systems. For verification two different experiments were conducted considering the system convenience.

In this study the eddy current conducting structures are divided into subdomains of unique dimensions of which the thickness is considered to be much smaller than the

corresponding skin depth and also much smaller than the other two dimensions. Subdomains are represented by their corresponding dc resistances and self-inductances assuming constant eddy current in each subdomain and, the inductive coupling relations between the subdomains and the gradient coils are solved to find subdomain-wise (position dependent) transient eddy current responses.

1.5.1 Coupled Circuit Analysis: 0.3 T Open MRI System

In open MRI systems, the gradient coils are of the planar type, consisting of an upper and a lower planar coil [51]. Also, the eddy current conducting structures have different geometrical shapes—for example, the local radio frequency (RF) shielding box has a cubic structure [51-52]. There is no direct traditional formula to compute inductive couplings between a planar gradient coil and different subdomains. As the formulation of a solid angle expression for three dimensions (3D) subtended by a two-dimensional (2D) current-carrying coil of arbitrary shape can be easily performed by simple mathematical manipulations in the Cartesian coordinates [53-57], we have implemented the solid angle form of Ampere's law [58] to compute the inductive coupling between planar gradient coil and any subdomain. In this study we have calculated the 3D solid angle formula for both Z-gradient (Gz coil) and X-gradient (Gx coil) coil patterns with the aim of computing coupling relations to subdomains in any position. We have also provided details of the solid angle calculation for both Z-gradient and X- or Y-gradient coils. For the calculation of solid angle for Z-gradient coil pattern (circular loop) we have followed the mathematical approaches explained in [53,55-56].

In case of X-gradient coil, because of asymmetric coil position compare to the magnet center, we have followed an efficient segmentation solid angle calculation approach by following the method explained by H. Gotoh, et al [57] in their calculation of solid angle at any field point

subtended by a rectangular slit. In our study we have found this approach mathematically less complex, faster in computer simulation, and easier to implement. We have also conducted free induction decay (FID) measurements of eddy currents by using an NMR probe designed at our laboratory to verify our simulation results. We have found a good agreement between the simulation and the experiment. Simulation of secondary magnetic field responses of X-gradient coil has also been performed and results are given for both transient and spatial responses of eddy current fields.

1.5.2 Coupled Circuit Analysis: 9.4 T Closed-Bore MRI System

We extended this solid angle coupled circuit analysis approach for the eddy current analysis of a 9.4 T narrow bore (54 mm inner diameter) superconducting magnet MRI system dedicated for MR microscopic study. In the superconducting magnet structure, the cylindrical bore and cryostat layers around the gradient coils have finite thickness and resistivity. For this reason, gradient magnetic fields can penetrate them and induce eddy currents with multiple decaying components that diffuse among different portions of the metal components with time constants that can be as long as 1s [16]. Specifically, long lasting eddy currents relative to the image acquisition period can be produced in the cold, highly conductive radiation shields of the magnet [9].

As coupled circuit method is based on the inductive coupling relations of the gradient coils and eddy current conducting structures, following the simulation on a 0.3 T open MRI system we implemented solid angle form of Ampere's law [58] for calculating the magnetic flux linkages between cylindrical gradient coils and subdomains considered in different conducting bores of the superconducting magnet. Similar circular solid angle calculation approach that was implemented for planar Gz coil was implemented for the calculation of inductive coupling

between cylindrical Gz coil and different subdomains. In case of cylindrical X-gradient coil, the coil loops in one quarter are in asymmetric position. Also the coil loop patterns have irregular geometrical shapes with 3-D curvatures [4,50] from the view point of spherical geometry. For this reason, in this study we divided the area of the loop of Gx coil into small rectangular sections on the cylindrical surface and calculated the solid angle of the rectangular sections considering the geometry and position of the coil loop in 3-D. In this study, the cylindrical Gz coil was represented as discrete circular loops and the cylindrical conducting structures are modeled into thin [7,22-23,46,48] circular ring-shaped subdomains. To simulate the eddy current induced by Gx coil we considered semicircular subdomains along the length of the bore as the net magnetic flux (hence, the inductive coupling) enclosed by a complete circular ring is zero for transverse (Gx or Gy) gradient coils. For experimental verification we followed the gradient eddy current measurement approach explained in [19] by V. J. Schmithorst et al in their calculation of automatic gradient preemphasis adjustment by measuring the magnitudes of eddy currents at various delay times (to measure the shift of gradient echo due to eddy current generated phase) after a test gradient pulse. We have found a good agreement between our simulation and measurement results.

Chapter 2

Methods and Materials

2.1 The Coupled Circuit Method – Basic Theory

In MRI systems, according to Faraday's law of electric induction [3], because of switching in the gradient signals eddy currents are induced in the surrounding conducting structures of the magnet with multiple decay time constants and amplitudes [8,16-17] depending on their electric, magnetic and structural properties, and positioning in MR magnetic circuits [9]. Mathematically it is convenient and more appropriate to express this kind of decaying responses of eddy currents as the sum of exponentials that is sometimes called as multiexponential characteristics of eddy currents [16,22]. Because of its multiexponential nature and dependency on the inductive coupling relations among the conducting structures, the eddy current responses can be numerically analyzed by representing the overall MR magnetic circuits as a stack of resistive-inductive (R-L) circuits [7,22-23] by dividing the conducting structures into inductively coupled small subdomains of unique dimensions of which at least one dimension is considered much smaller than the other two dimensions and thickness is much smaller than the skin depth of the corresponding signal frequency [4,7,22] so that the eddy current can be assumed to have constant amplitude in each subdomain. It is also assumed that the overall system response is linear [4]. System of first order differential equations is formulated from these networks of resistive-inductive series circuits. Eddy current transient responses in different subdomains at different locations can be easily found by solving this system of first order differential equations. In 1984, M. J. Sablik et al. first formulated this concept into a coupled circuit numerical analysis method. Further works [10,46-48] have proven this approach as an efficient, fast, and

computationally less complex numerical analysis method than the conventional methods for analyzing the eddy current characteristics in MRI systems.

To illustrate the coupled circuit approach, let us consider a small network of R-L circuits combining gradient coil and three subdomains as is shown in Fig. 2.1. The gradient coil and each of the subdomains are represented by their corresponding resistances (R) and inductances (L). The inductive couplings between gradient coil and subdomains and, between the subdomains are represented respectively by M_{is} and M_{ii}, where i is the subdomain number. In Fig. 2.1, M_{11}, M_{22}, M_{33} are represented by L_1, L_2, L_3 respectively.

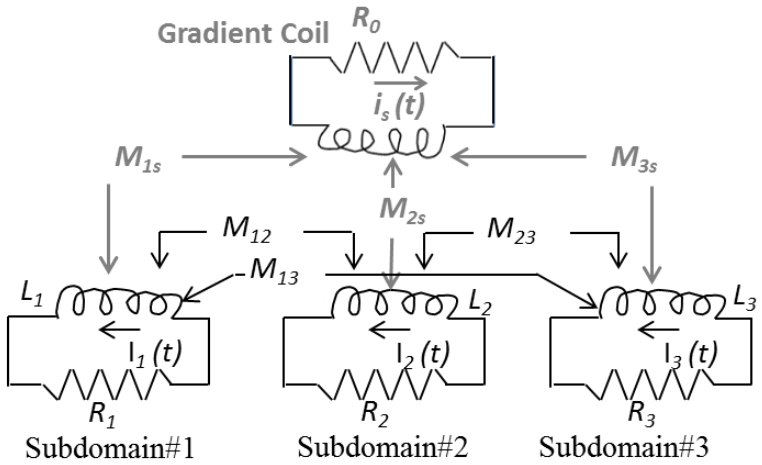

Fig. 2.1. Coupled resistive-inductive (R-L) circuit representation considering gradient coil and three subdomains taken in eddy current conducting structure. Light black notations are the parameters related to gradient coil and black notations are related to the subdomains.

Following the basic R-L circuit characteristic response [23], eddy current in subdomain #1 can be calculated by the following coupling differential equation:

$$L_1 \frac{dI_1(t)}{dt} + R_1 I_1(t) = -M_{1s} \frac{di_s(t)}{dt} - M_{12} \frac{dI_2(t)}{dt} - M_{13} \frac{dI_3(t)}{dt}$$

$$\text{or}, L_1 \frac{dI_1(t)}{dt} + M_{12} \frac{dI_2(t)}{dt} + M_{13} \frac{dI_3(t)}{dt} + R_1 I_1(t) = -M_{1s} \frac{di_s(t)}{dt}$$

Similarly eddy currents in subdomains #2 and #3 can be calculated respectively by the following equations:

$$L_2\frac{d\mathrm{I}_2(t)}{dt}+M_{21}\frac{d\mathrm{I}_1(t)}{dt}+M_{23}\frac{d\mathrm{I}_3(t)}{dt}+R_2\mathrm{I}_2(t)=-M_{2s}\frac{di_s(t)}{dt}$$

$$L_3\frac{d\mathrm{I}_3(t)}{dt}+M_{31}\frac{d\mathrm{I}_1(t)}{dt}+M_{32}\frac{d\mathrm{I}_2(t)}{dt}+R_3\mathrm{I}_3(t)=-M_{3s}\frac{di_s(t)}{dt}$$

As the above three equations have linear dependency among them, we can solve them as a system of equations which can be represented in matrix form as:

$$\begin{pmatrix}L_1 & M_{12} & M_{13}\\ M_{21} & L_2 & M_{23}\\ M_{31} & M_{32} & L_3\end{pmatrix}\begin{pmatrix}\mathrm{I}_1(t)\\ \mathrm{I}_2(t)\\ \mathrm{I}_3(t)\end{pmatrix}+\begin{pmatrix}R_1 & 0 & 0\\ 0 & R_2 & 0\\ 0 & 0 & R_3\end{pmatrix}\begin{pmatrix}\mathrm{I}_1(t)\\ \mathrm{I}_2(t)\\ \mathrm{I}_3(t)\end{pmatrix}=-\begin{pmatrix}M_{1s}\\ M_{2s}\\ M_{3s}\end{pmatrix}\frac{di_s(t)}{dt}$$

For N number of subdomains the above equation becomes [4,7,10,22-23]:

$$\mathbf{M}_{ii}\frac{d\mathbf{I}(t)}{dt}+\mathbf{R}_i\mathbf{I}(t)=-\mathbf{M}_{is}\frac{di_s(t)}{dt}\text{, where}$$

$$\mathbf{M}_{ii}=\begin{pmatrix}L_1 & M_{12} & . & M_{1n}\\ M_{21} & L_2 & . & M_{2n}\\ . & . & . & .\\ M_{n1} & M_{n2} & . & L_n\end{pmatrix}\ ;\quad \mathbf{M}_{is}=\begin{pmatrix}M_{1s}\\ M_{2s}\\ .\\ M_{ns}\end{pmatrix}\ ;\quad \mathbf{R}_i=\begin{pmatrix}R_1 & 0 & . & 0\\ 0 & R_2 & . & 0\\ . & . & . & .\\ 0 & 0 & . & R_n\end{pmatrix}\ ;\quad \text{in which,}$$

$L_1,\ L_2,\ \ldots\ldots, L_n$ are the self-inductances of the subdomains (which have been replaced for $M_{11},\ M_{22},\ \ldots\ldots, M_{nn}$ in the $\mathbf{M}_{ii}$ matrix); $M_{12},\ M_{13},\ \ldots\ldots, M_{1n}$ are the mutual inductances between the subdomains; $M_{1s},\ M_{2s},\ \ldots\ldots, M_{ns}$ are the mutual couplings between the gradient coil and the subdomains; and $R_1,\ R_2,\ \ldots\ldots, R_n$ are the resistances of the subdomains; $i_s(t)$ is the gradient coil current which is represented in our work as trapezoidal signal in the time-domain with equal ramp-up and ramp-down time and constant flat-top current of duration much higher so that the eddy current signal can decay within this period. The signal representation can be expressed as

$$i_s(t) = \begin{cases} 0, & t \le t_1 \\ \dfrac{i_o(t - t_1)}{t_2 - t_1}, & t_1 \le t \le t_2 \\ 1, & t_2 \le t \le t_3 \\ \dfrac{i_o(t_3 - t)}{t_4 - t_3}, & t_3 \le t \le t_4 \\ 0, & t_4 \le t \end{cases}$$

where, i_o is the maximum current and parameter t_1, t_4 define the start and end point of the trapezoidal signal and, t_2, t_3 locate the shoulders of the signal (as is illustrated in Fig. 2.2). **I**(t) is the eddy current vector with dimensions equal to the number of subdomains considered. In this study, we have applied the Eigen matrix concepts of solving differential equations to simplify and speed up the entire calculation process. The details of the Eigen method approach is explained below considering both the homogeneous and nonhomogeneous form of differential equations.

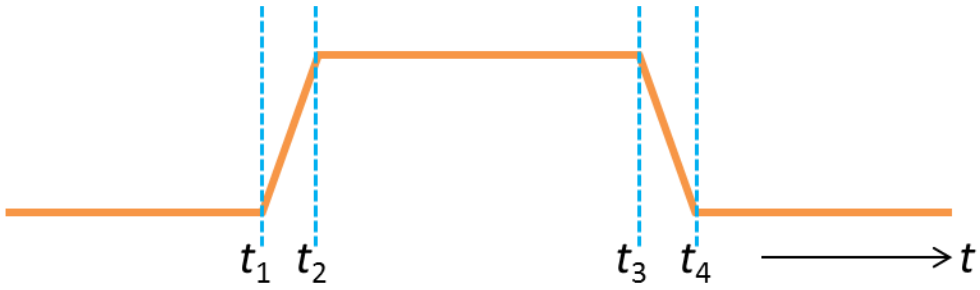

Fig. 2.2. An ideal trapezoidal shape signal. Here, t_1, t_4 define the start and end point of the signal and, t_2, t_3 locate the shoulders of the signal.

2.2 Simplification by the Eigen Method

The coupled first order differential equation is expressed here again for clarity:

$$\mathbf{M}_{ii} \frac{d\mathbf{I}(t)}{dt} + \mathbf{R}_i \mathbf{I}(t) = -\mathbf{M}_{is} \frac{di_s(t)}{dt}$$

With some simple mathematical manipulations, we can express the above system of ordinary differential equations as

$$\frac{d\mathbf{I}(t)}{dt} = \mathbf{A}\mathbf{I}(t) + \mathbf{B}\frac{di_s(t)}{dt}$$

where, $\mathbf{A} = -\mathbf{M}_{ii}{}^{-1}\mathbf{R}_i$ and $\mathbf{B} = -\mathbf{M}_{ii}{}^{-1}\mathbf{M}_{is}$. For the constant flattop portion of the gradient signal the second term ($\frac{di_s(t)}{dt}$) of the right hand side of above equation is zero and it becomes a homogeneous system of differential equations:

$$\frac{d\mathbf{I}(t)}{dt} = \mathbf{A}\mathbf{I}(t)$$

On the other hand, for the ramp-up or ramp-down duration of the gradient signal (Fig 2.2), $\frac{di_s(t)}{dt}$ is not zero and the system of differential equations becomes a nonhomogeneous differential equation problem. In this study, we treat the homogeneous case by implementing decoupling solution method and nonhomogeneous case by fundamental matrix method as is explained below.

Case 1: Homogeneous: To solve a homogeneous linear system of differential equations with constant coefficients and initial values like,

$$\frac{d\mathbf{I}(t)}{dt} = \mathbf{A}\mathbf{I}(t), \qquad \mathbf{I}(t_0) = \mathbf{I}_0,$$

the solution method becomes:

(i) Perform the change of variables:

$$\mathbf{I}(t) = \mathbf{C}\mathbf{z}(t),$$

where, $\mathbf{z}(t)$ is the new variable and $\mathbf{C}$ is invertible matrix.

(ii) The differential equation will become as:

$$\frac{d\mathbf{z}(t)}{dt} = \mathbf{D}\mathbf{z}(t)$$

where,

$$\mathbf{D} = \mathbf{C}^{-1}\mathbf{A}\mathbf{C} \quad \leftrightarrow \quad \mathbf{A} = \mathbf{C}\mathbf{D}\mathbf{C}^{-1}$$

(iii) Compute the eigenvalues and eigenvectors of the coefficient matrix, $\mathbf{A}$.

(iv) Use the eigenvalues and eigenvectors of **A** to respectively construct the diagonal matrix **D** and the change of basis matrix, **C**.

(v) Write down the general solution of the decoupled system,

$$\frac{d\mathbf{z}(t)}{dt} = \mathbf{D}\mathbf{z}(t) \quad \rightarrow \quad \mathbf{z}(t) = \begin{bmatrix} c_1 e^{\lambda_1 t} \\ \vdots \\ c_n e^{\lambda_n t} \end{bmatrix}$$

c_1**……,** c_n are the integration coefficients which are solved by using initial values, and λ_1**,** λ_2**,** **……,** λ_n are the Eigen values of **A**.

(v) Initial value can be calculated as: $(t_o) = \mathbf{C}^{-1}\mathbf{I}(t_o)$; (from equation $\mathbf{I}(t) = \mathbf{C}\mathbf{z}(t)$), where $I_n(t_0)$ is the initial value (at $t = t_0$) of eddy current in the *n*-th subdomain.

(vi) The integration coefficient for *n*-th subdomain will become as,

$$c_n = z_n(t_o)e^{-\lambda_n t_o}$$

(vii) $\mathbf{z}(t)$ is solved:

$$\mathbf{z}(t) = \begin{bmatrix} c_1 e^{\lambda_1 t} \\ \vdots \\ c_n e^{\lambda_n t} \end{bmatrix}$$

(vii) The solution of the original (coupled) system will be,

$$\mathbf{I}(t) = \mathbf{C}\mathbf{z}(t).$$

Case 2: Nonhomogeneous: To find the solution to the initial value problem of the nonhomogeneous equations

$$\frac{d\mathbf{I}(t)}{dt} = \mathbf{A}\mathbf{I}(t) + \mathbf{E}(t), \qquad \mathbf{I}(t_0) = \mathbf{I}_0,$$

where $\mathbf{E}(t) = \mathbf{C}^{-1}\mathbf{B}\frac{di_s(t)}{dt}$**,** we implement the fundamental matrix method:

(i) The fundamental matrix can be expressed as

$$\boldsymbol{\Phi}(t) = \begin{bmatrix} v_{11}e^{\lambda_1 t} & v_{12}e^{\lambda_2 t} & \ldots . v_{1n}e^{\lambda_n t} \\ \vdots & \vdots & \vdots \\ v_{n1}e^{\lambda_1 t} & v_{n2}e^{\lambda_2 t} & \ldots . v_{nn}e^{\lambda_n t} \end{bmatrix},$$

where $\boldsymbol{v_1}(v_{11}, v_{21},..., v_{n1})$, $\boldsymbol{v_2}$ $(v_{12}, v_{22},..., v_{n2})$, ..., $\boldsymbol{v_n}$ $(v_{1n}, v_{2n},..., v_{nn})$ are the associated eigenvectors, and $\lambda_1, \lambda_2, \ldots, \lambda_n$ are the eigenvalues of the corresponding homogeneous equation.

(ii) The solutions of the nonhomogeneous equations can be given by

$$\mathbf{I}(t) = \boldsymbol{\Phi}(t)\boldsymbol{\Phi}(t_0)^{-1}\mathbf{I}(t_0) + \int_{t_0}^{t} \boldsymbol{\Phi}(t)\boldsymbol{\Phi}(s)^{-1}\,\mathbf{E}(s)ds$$

2.3 Coupled Circuit Modeling: 0.3 T Open MRI System

In this study, at first we implemented the coupled circuit method to simulate the eddy current responses in an open compact 0.3 T MRI system (as shown in Fig. 2.3) that was developed for skeletal age assessment in children [51]. In open MRI system, the gradient coils are of the planar type consisting of an upper and a lower coil positioned in the gap between the magnet poles (as is shown schematically in Fig. 2.4). Let us consider the eddy current responses in the cubic RF shielding box. We can consider the upper and lower coils as a single eddy current generating source. Following the coupled circuit approach we subdivide the brass plates in the RF box into several subdomains along the thickness and length of each plate [7,22–23].

To consider the skin effect of eddy current, at first, each conducting structure is subdivided into a number of ideally infinitely thin sublayers so that enough sublayers are considered to represent the skin depth more accurately [4]. For practical numerical calculation purposes, a sufficient number of sublayer is considered, so that the eddy currents in each layer can be assumed as constant. But considering a finite number of sublayers would necessarily

introduce some errors in the simulation results that decrease with decreasing sublayer thickness [47]. Following the approach in references [4,22,47], we have considered the thickness to be less

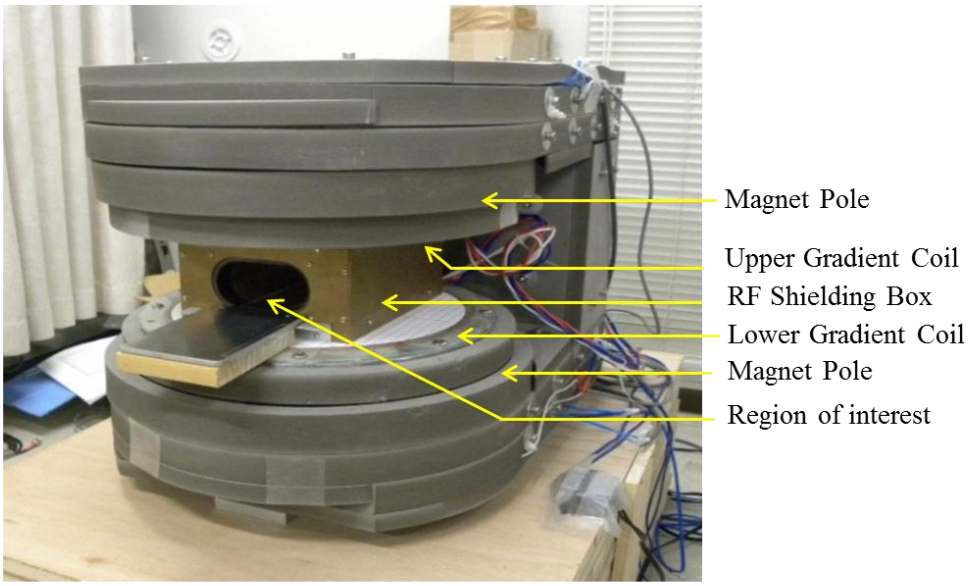

Fig. 2.3. 0.3 T Open Compact MRI System for child growth measurement.

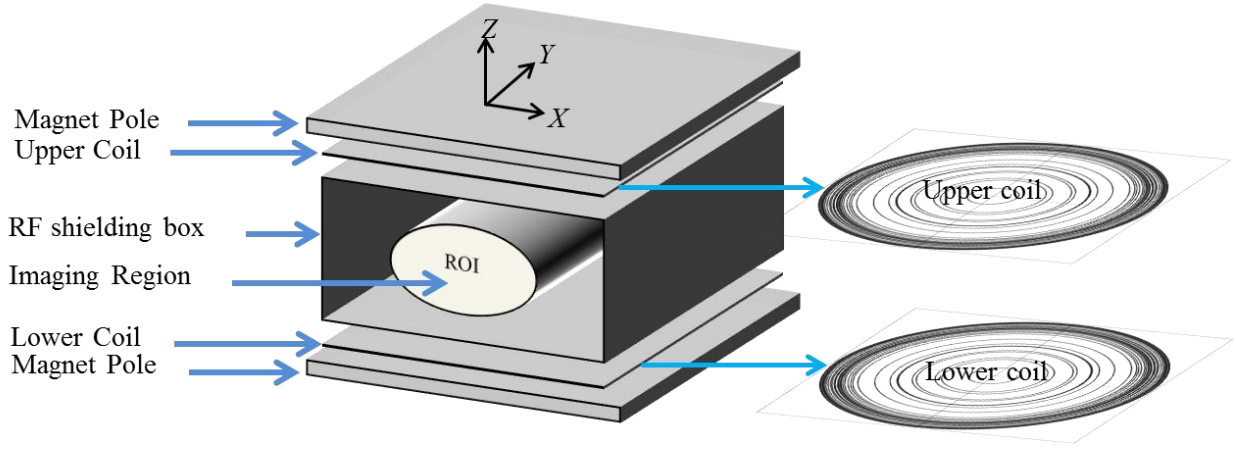

Fig. 2.4. Schematic representation of the 0.3 T Open Compact MRI System. The gradient coil is consisted of upper and lower planar coils.

than one-tenth of the skin depth, δ. For high frequency and/or high conductivity, the formula we took for δ can be expressed [59] as

$$\delta = \sqrt{\frac{2}{\mu\omega\sigma}}$$

where, μ is the permeability, ω is the angular frequency, and σ is the conductivity. Each sublayer is again divided into several subdomains along the length or width. Fig. 2.5 illustrates the division of a conducting plate (e.g., upper plate) into subdomains. The conducting structure is divided into sublayers and subdomains along thickness (along Z-axis) and length or width (along Y- or X-axis), respectively, so that the thickness d is much smaller than the skin depth of the corresponding signal frequency. For Gx coil, subdomains in each sublayer are taken along the width or along the X-axis. Division along the Y-axis (considering Gx coil) would result in zero net flux induced by the coil to a subdomain as the magnetic flux have similar but opposite values on both sides of X-axis from the center. In case of Gy coil subdomain division should be done along the Y-axis. Because the current in each subdomain is considered to be constant, we have assumed dc resistance for each subdomain. The resistance of each subdomain is then calculated by [48],

$$R = \rho\frac{l}{wt}$$

where, ρ is the resistivity and l, w, and t are the length, width, and thickness of each subdomain, respectively. The self- and mutual inductances among the subdomains are computed by applying the simple formulas taken from the reference [60].

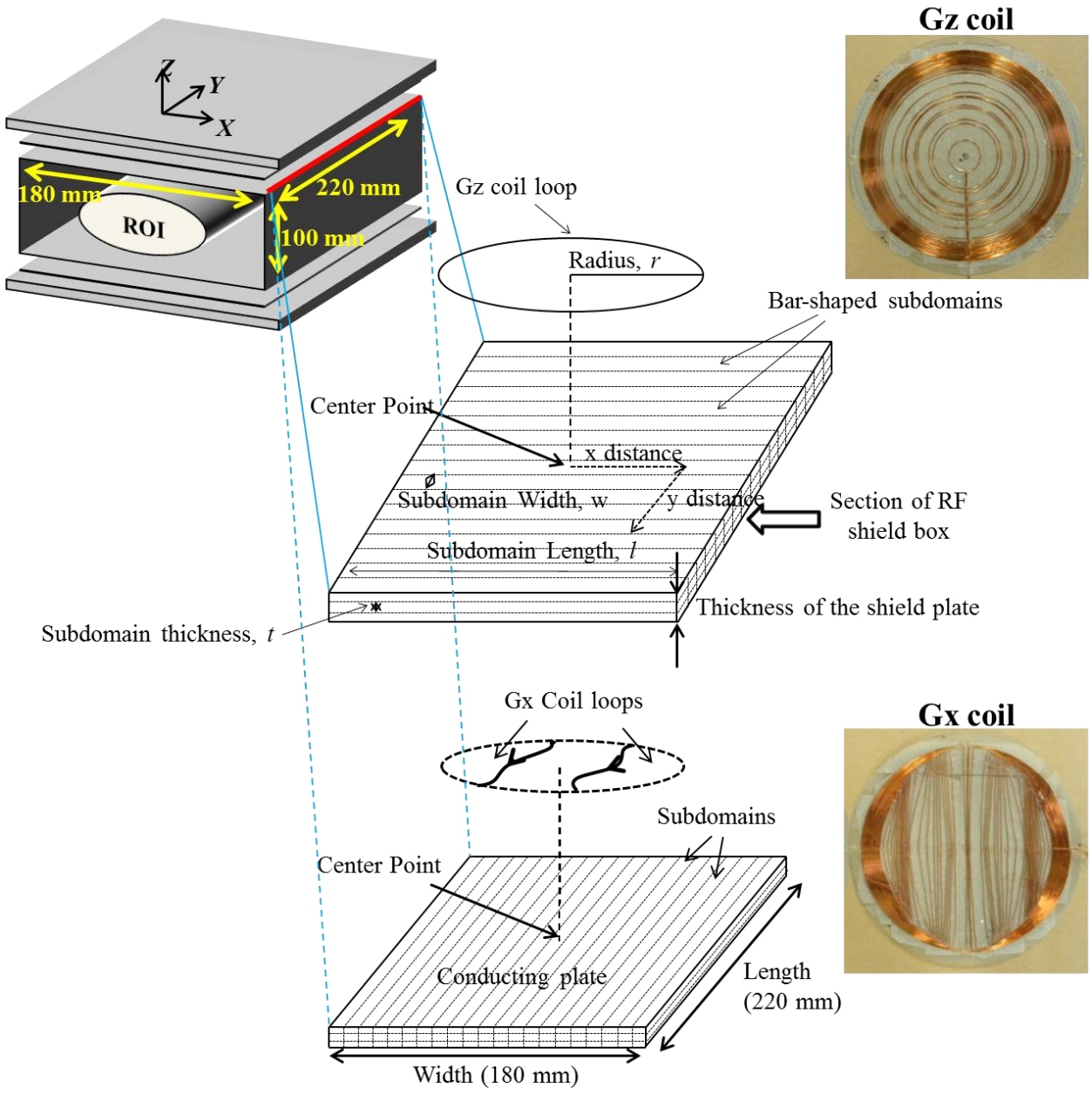

Fig. 2.5. Schematic representation of modeling the conducting plates into subdomains considering both longitudinal (Gz) and transverse (Gx) coils. Details of the parameters dimensions are given in this illustration.

The self-inductance of a subdomain was computed by the following formula [60],

$$\frac{\mu_0}{2\pi} l \left[\mathrm{Log}\left(\frac{2l}{0.2235(t+w)} \right) - 1 + \frac{0.2235(t+w)}{l} \right]$$

where, μ_0 is the magnetic permeability, l is the length, w is the width, and t is the thickness of each subdomain. And the mutual inductance between the subdomains was computed by the following expression [60]:

$$\frac{\mu_0}{2\pi} l \left[\mathrm{Log}\left(\frac{l}{d} + \sqrt{1 + \frac{l^2}{d^2}} \right) - \sqrt{1 + \frac{d^2}{l^2}} + \frac{d}{l} \right]$$

Here, d is the geometric mean distance between subdomains, which is equal to the distance between the centers.

The Z-gradient coil has a combination of circular current loops wound onto a surface of fiber-reinforced plastic (FRP) plate with the diameter optimized using a genetic algorithm [51]. To calculate the inductive coupling between the planar coils (upper and lower coils) and any subdomain, we implemented the solid angle form of Ampere's law, according to which the magnetic flux density (B) is proportional to the gradient of the solid angle (Ω) subtended by an arbitrary loop carrying a current, i_{coil} [58]:

$$\mathrm{B} = \frac{-\mu_o i_{coil} \nabla \Omega}{4\pi}$$

Here, ∇ is the gradient operator. In order to calculate the flux linkage of the gradient coil to subdomains at any position we need to formulate the solid angle expression considering any location in the three dimensional space. In our analysis, we have formulated the solid angle expression in Cartesian coordinate considering all three axes, X, Y, and Z for both Gz and Gx type coil loops by following the works done in References [53,55-57]. Because of cylindrical symmetry we have followed a simple analytical solid angle calculation approach for Gz coil

(circular current loop) by following the methods given in references [53,55-56]. But in case of Gx coil the current loops are in asymmetric position with respect to the magnet center. To consider this fact, we have applied a simple rectangular segmentation approach to calculate the solid angle of Gx coil at any position in the region of interest (ROI) by following the method given in reference [57]. Details of the calculation methods are explained in the following sections. Fig. 2.6 (a) and (b) show the schematic diagram of the solid angle approach in coupled circuit method for loops in upper coil and subdomains of the upper conducting plate of the RF shield box considering Gz coil and Gx coil, respectively. If B_{dom} is the average magnetic flux density in each subdomain generated by all the current loops in the gradient set carrying an equal current i_{coil}, then the total flux across each subdomain of area A_{dom} and, hence, the inductive coupling between the gradient coil and each subdomain (M_{is}) [3] can be calculated by

$$M_{is} = {B_{dom}A_{dom}}/{i_{coil}}$$

As for the planar Z-gradient coil, it has two sets of similar coils near the magnet poles (as shown in Fig. 2.4). Since current circulations in these two layers of coils are opposite in direction [14] the solid angle in the region of interest (ROI) will be of opposite sign – for anti-clockwise current circulation the solid angle is positive and for clockwise circulation it is negative [58]. If M_{ir} is the flux linkage between the *r*-th coil loop and *i*-th subdomain, then the total flux linkage to that subdomain from *n* number of loops will be

$$\sum_{r=1}^{r=n} M_{ir}$$

At any subdomain in between the magnet gap, these opposite flux linkages - induced from all of the coil loops both from the upper and the lower coil sets - are added to get total flux

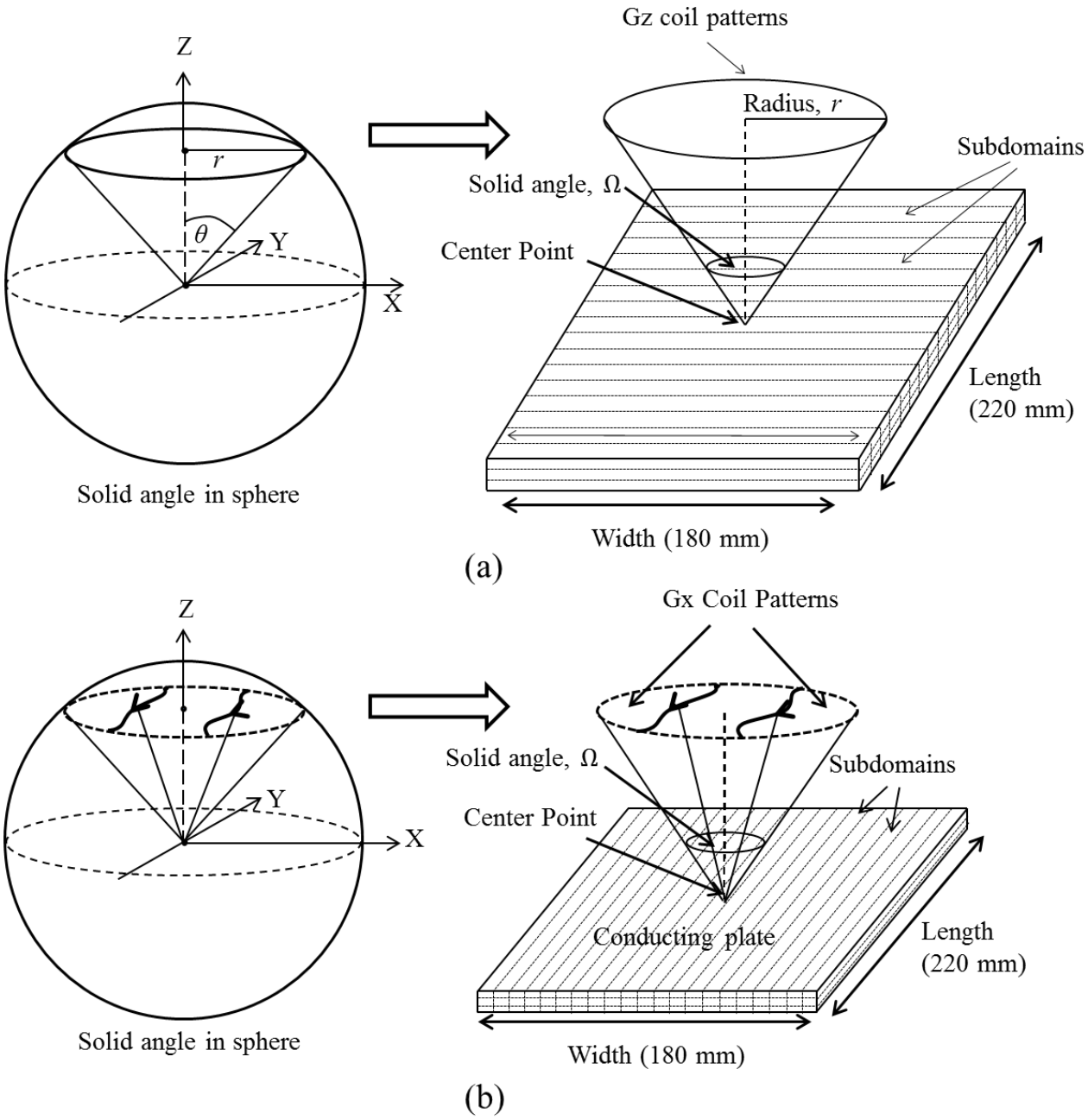

Fig. 2.6. Schematics of solid angle coupled circuit modeling considering (a) Gz and (b) Gx coil loops.

linkage of Gz coil to that subdomain. In this way, inductive coupling between Z-gradient coil and all of the subdomains are calculated.

In case of X-gradient coil, it also has upper and lower layer coils near the magnet poles. In addition, in each layer there have two sets of the similar coil patterns with clockwise and anti-clockwise current circulations [50]. Flux linkages of Gx coil to any subdomain in the magnet gap should consider contribution of flux linkages from these four sets of coil loops. The sign of the solid angles are considered according to the current circulation directions mentioned above. Once we have calculated all the matrices of inductances and resistances (M_{ii}, M_{is}, and R_{ii}) for a network of coupled eddy current conducting subdomains, we can implement them in the coupled differential equations to get the transient response of eddy current in different subdomains at different locations.

2.3.1 Solid Angle Calculation for Z-gradient coil pattern

Following the work of F. Paxton [53] and E. Galiano et al. [55], we calculated the solid angle formula for the circular-type coil for three dimensions. The basic equation of solid angle formulation can be expressed as [53]

$$\Omega = \int \frac{\mathbf{n}.\mathbf{ds}}{z^2}$$

where ds is the infinitesimal area of the coil and $\mathbf{n}.\mathbf{ds}$ is the area of the projection of ds onto the plane perpendicular to z, as shown in Fig. 2.7(b). As a starting point, we took an expression derived from the equation given in [58]. The expression that describes the solid angle subtended by a circular coil of radius r at the center of a sphere is:

$$\Omega = 2\pi(1 - \cos\theta)$$

where θ represents the apex angle and cosθ can be expressed from Fig. 2.7(b) as $\frac{z}{\sqrt{z^2+r^2}}$. We can also express the above equation as

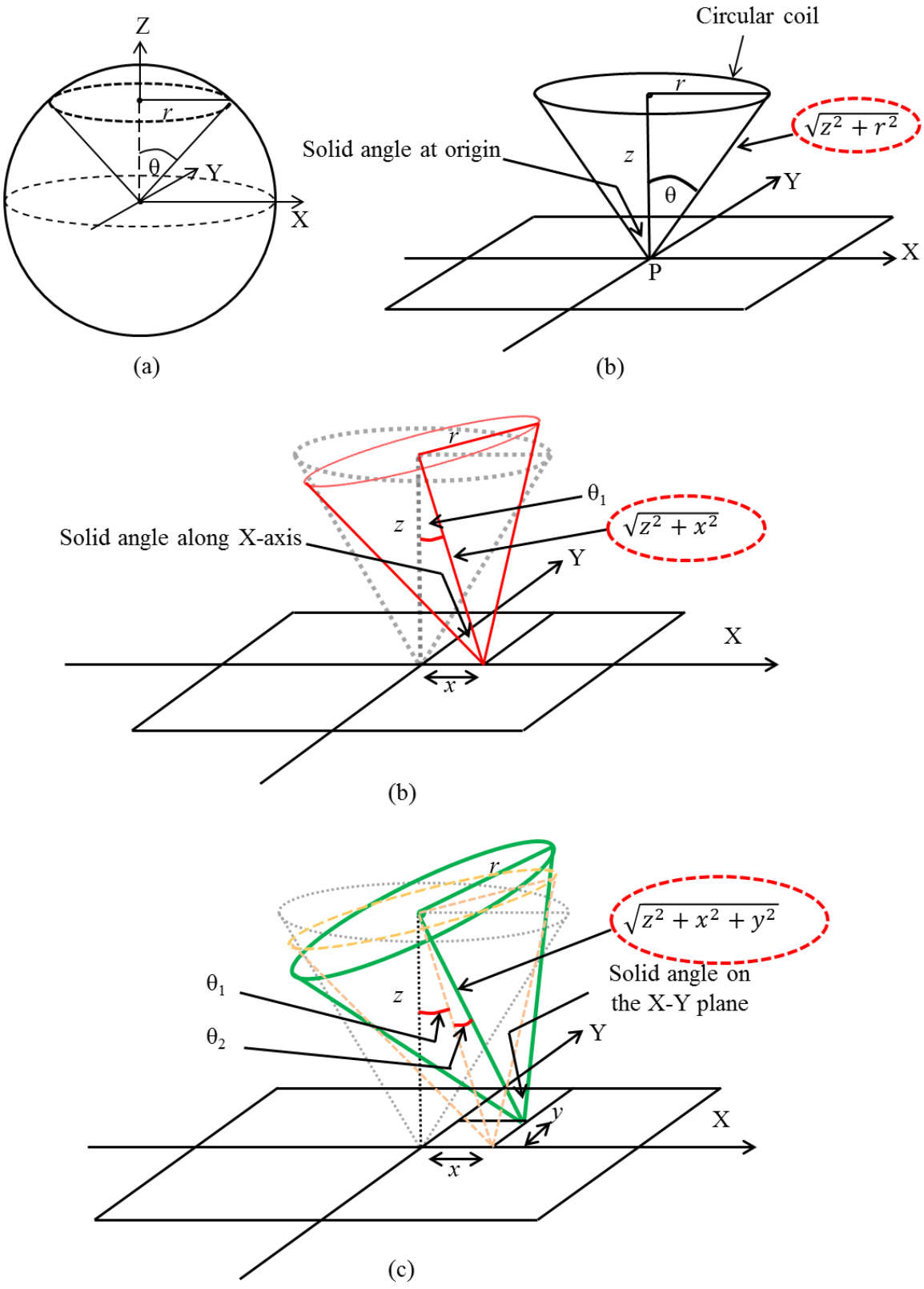

Fig. 2.7. (a) Solid angle in a sphere; (b) Solid angle of circular loop at the center of the coordinate; (c) Solid angle along the X-axis; (d) Solid angle at any point.

$$\Omega = 2\pi\left(1 - \frac{\mathrm{z}}{\sqrt{z^2 + r^2}}\right)$$

To obtain an expression for the solid angle along the X-axis, two factors must be taken into account: first, the point at *x* is now at a distance of $\sqrt{z^2 + x^2}$ from the center of the coil, and second, from this viewpoint the coil appears to be skewed at an angle of θ_1 with respect to the normal (see the black dashed lines in Fig. 2.7(c)). If we take the projection $(\cos\theta_1)$ of the skewed coil at the original position of the coil, we need to multiply $\frac{\mathrm{z}}{\sqrt{z^2+x^2}}$ with the above equation. The equation along the X-axis then becomes

$$\Omega = 2\pi\left(1 - \frac{\sqrt{z^2 + x^2}}{\sqrt{z^2 + x^2 + r^2}}\right) \times \frac{\mathrm{z}}{\sqrt{z^2 + x^2}}$$

Now, if we skew the X-skewed coil along the Y-axis again (as shown by the red circle in Fig. 2.7(d)), z will become $\sqrt{z^2 + x^2 + y^2}$ and we have to multiply the projection $(\cos\theta_2)$ of the Y-skewed coil, $\frac{\sqrt{z^2+x^2}}{\sqrt{z^2+x^2+y^2}}$, with the above equation. Therefore, the final equation can be expressed as

$$\Omega = 2\pi\left(1 - \frac{\sqrt{z^2 + x^2 + y^2}}{\sqrt{z^2 + x^2 + y^2 + r^2}}\right) \times \frac{\mathrm{z}}{\sqrt{z^2 + x^2}} \times \frac{\sqrt{z^2 + x^2}}{\sqrt{z^2 + x^2 + y^2}}$$

$$or\ \ \Omega = 2\pi\left(\frac{\mathrm{z}}{\sqrt{z^2 + x^2 + y^2}} - \frac{\mathrm{z}}{\sqrt{z^2 + x^2 + y^2 + r^2}}\right)$$

2.3.2 Solid Angle Calculation for planar X- or Y-gradient coil pattern

The solid angle of Gx coil is calculated by following the research work done by H. Gotoh, et al [57] for a rectangular slit. At first we will explain in brief on the solid angle of a rectangle at a point on Z-axis. Fig. 2.8(a), illustrates the schematic of solid angle subtended at P (0, 0, *h*) by a rectangle OERC with side lengths *a* and *b*. The solid angle subtended by this rectangle at the point P can be represented by [57],

$$\Omega = h\int_0^a dx\int_0^b \frac{dy}{(x^2+y^2+z^2)^{\frac{3}{2}}}$$

The solution of this double integral has been given as [57],

$$\Omega = \tan^{-1}\frac{ab}{h(a^2+b^2+h^2)^{\frac{1}{2}}}$$

Now if we consider the field point P at (x_2, y_2, h) as is shown in Fig 2.8(b), the solid angle of the rectangle OERC (constructed by the red solid lines) can be written as,

$$\Omega = \tan^{-1}\frac{(x_1-x_2)(y_1-y_2)}{h((x_1-x_2)^2+(y_1-y_2)^2+h^2)^{\frac{1}{2}}}$$

To consider solid angle of a rectangle at any point, let us consider solid angle subtended at an arbitrary observation point P (x_p, y_p, z_p) by the rectangle OERC (see Fig. 2.8(c)). The solid angle formula will become as

$$\Omega = \tan^{-1}\frac{(x_1-x_p)(y_1-y_p)}{h\left((x_1-x_p)^2+(y_1-y_p)^2+h^2\right)^{\frac{1}{2}}}$$

The solid angle of a rectangular section (CRE'D) of one coil loop (illustration given in Fig. 2.9) can be calculated by the following approach:

$$\Omega_{\mathrm{CRE'D}} = \Omega_{\mathrm{OEE'D}} - \Omega_{\mathrm{OERC}}$$

The formula will become as:

$$\Omega_{\mathrm{CRE'D}} = \tan^{-1}\frac{(x_1-x_p)(y_2-y_p)}{z_p\left[(x_1-x_p)^2+(y_2-y_p)^2+z_p\right]^{\frac{1}{2}}} - \tan^{-1}\frac{(x_1-x_p)(y_1-y_p)}{z_p\left[(x_1-x_p)^2+(y_1-y_p)^2+z_p\right]^{\frac{1}{2}}}$$

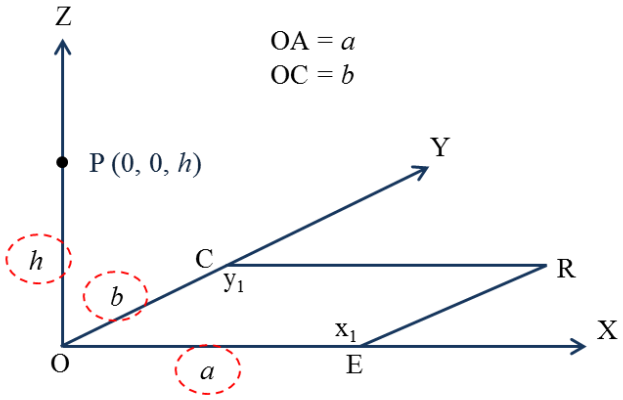

Solid angle calculation at P (0, 0, h)

(a)

Solid angle for Fig (a),

$$\Omega = \tan^{-1} \frac{ab}{h(a^2 + b^2 + h^2)^{\frac{1}{2}}}$$

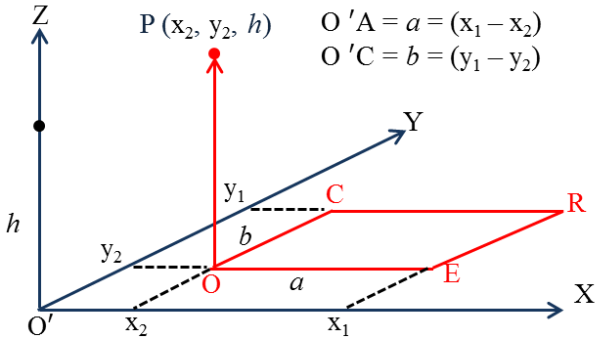

Solid angle calculation at P (x_2, y_2, h)

(b)

Solid angle for the Red rectangle (Fig (b)),

$$\Omega = \tan^{-1} \frac{(x_1 - x_2)(y_1 - y_2)}{h((x_1 - x_2)^2 + (y_1 - y_2)^2 + h^2)^{\frac{1}{2}}}$$

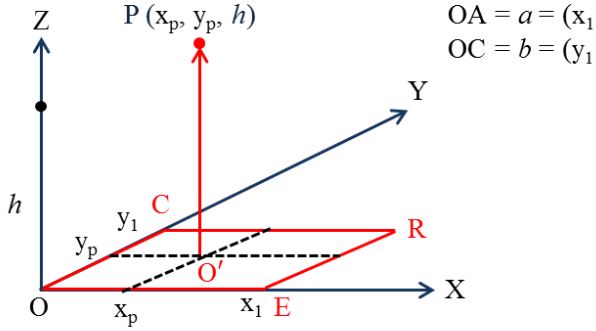

Solid angle calculation at P (x_p, y_p, h)

(c)

Solid angle at P in Fig. (c) for OERC,

$$\Omega = \tan^{-1} \frac{(x_1 - x_p)(y_1 - y_p)}{h\left((x_1 - x_p)^2 + (y_1 - y_p)^2 + h^2\right)^{\frac{1}{2}}}$$

Fig. 2.8.Rectangular solid angle calculation: (a) solid angle subtended at any point along Z-axis; (b) solid angle at any point along Z-axis with the shifting of X-Y coordinates; (c) solid angle at any point P (x_p, y_p, h) without coordinate shifting.

The solid angle subtended by the section of coil in first quadrant, CB'F'N will become as the sum of three rectangular solid angles (approximately) subtended by CB'E'D, DE'F'G and GF'H'I, respectively:

$$\Omega_{CB'F'N} = (\Omega_{OEE'D} - \Omega_{OERC}) + (\Omega_{OFF'G} - \Omega_{OFPD}) + (\Omega_{OHH'I} - \Omega_{OHQG})$$

Total solid angle of the Gy coil (arc MNB') will be double of the above equation

$$\Omega_{Total} = 2\Omega_{B'F'NC}$$

In this fashion we can divide the arc of any gradient coil into enough rectangular sections and calculate the solid angle with some approximations.

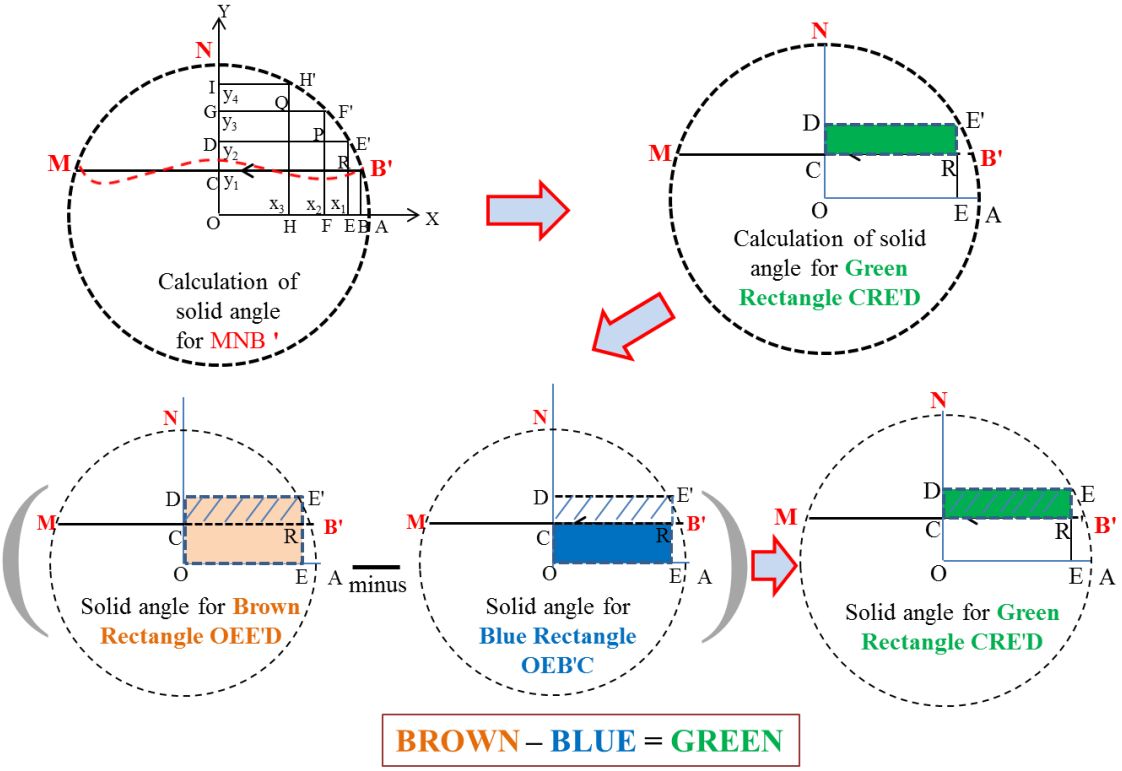

Fig. 2.9.Rectangular solid angle segmentation approach implemented to calculate the solid angle of Gx coil loops. To calculate the solid angle of green rectangular area, solid angle of blue area is subtracted from solid angle of brown area.

2.4 Coupled Circuit Modeling: 9.4 T Closed-Bore MRI System

In this study, we also simulated the eddy current responses in the inner four cylindrical conducting bores of a 9.4 T narrow-bore (54 mm diameter) superconducting magnet MRI system. The superconducting magnet and a schematic of its internal four cylindrical conducting bores are shown in Fig. 2.10 (a) and (b), respectively. Throughout this thesis, these four cylindrical bores will be mentioned as the innermost bore (warm bore or room temperature bore), second bore (77 K bore (liquid nitrogen)), third bore (4.2 K (liquid helium)) and fourth bore (4.2 K (liquid helium)) with their increasing diameters. The material properties and structural dimensions are listed in Table 1.

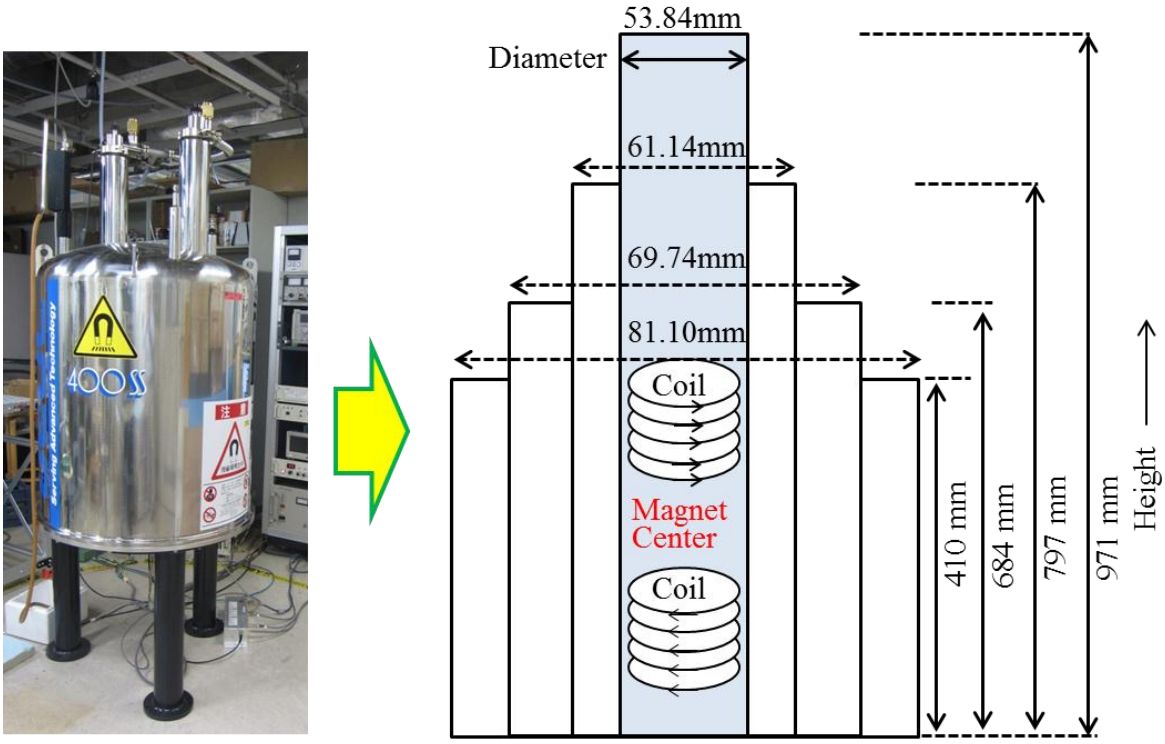

Fig. 2.10. (a) 9.4 T vertical narrow bore (54 mm i.d.) superconducting MRI magnet; (b) Schematic representation of the innermost four bores of the magnet.

Table 1

Bore #	Materials	Diameter (mm)	Thickness (mm)	Temperature	Temperature Coefficient (/K)	Resistivity, ρ (Ω-m)
1st Bore	Cu (C1220)	53.84	1.63	293 K	.0039	$2.0284X10^{-8}$
2nd Bore	Cu (C1220)	61.14	1.63	77 K	.0039	$1.1009X10^{-8}$
3rd Bore	Cu (C1220)	69.74	1.63	4.2 K	.0039	$0.9545X10^{-8}$
4th Bore	Al (AC4C)	81.1	3.00	4.2 K	.0043	$1.9273X10^{-8}$

To model the cylindrical bores into subdomains we first divide each bore into thin cylindrical sublayers along the thickness and, each sublayer is again divided into ring-shaped subdomains along the length (along the Z-axis). Fig. 2.11 illustrates the coupled circuit modeling approach of a conducting bore for eddy current simulation induced by Z-gradient coil. To calculate the resistance of each ring-shaped subdomain the following formula was followed:

$$R = \rho \frac{2\pi a}{wt}$$

where, ρ is the resistivity and a, w, and t are the radius, width, and thickness of each subdomain, respectively. The self-inductance $(L_1, L_2, \ldots\ldots, L_n)$ was computed by the following formula given by Rayleigh [60]:

$$L = \mu_o a \left[\mathrm{Log}\frac{8a}{w} - \frac{1}{2} + \frac{w^2}{32a^2}\left(\mathrm{Log}\frac{8a}{w} + \frac{1}{4}\right)\right]$$

where, a is the radius of the circular ring, w is the width of the ring. To compute inductive couplings between any two subdomains ($M_{12}, M_{13}, \ldots\ldots, M_{1n} \ldots$), we implemented the following formula [59]:

$$M_{ii} = 2\mu_o \sqrt{\frac{a_1 a_2}{k}} \left(\left(1 - \frac{k}{2}\,\mathrm{EllipticK}(k)\right) - \mathrm{EllipticE}(k) \right)$$

$$\text{with, } k = \frac{4a_1 a_2}{((z_1 - z_2)^2 + (a_1 + a_2)^2)}$$

where, a_1 and a_2 are the radii of two different circular rings and z_1, z_2 are their respective positions along the Z-axis.

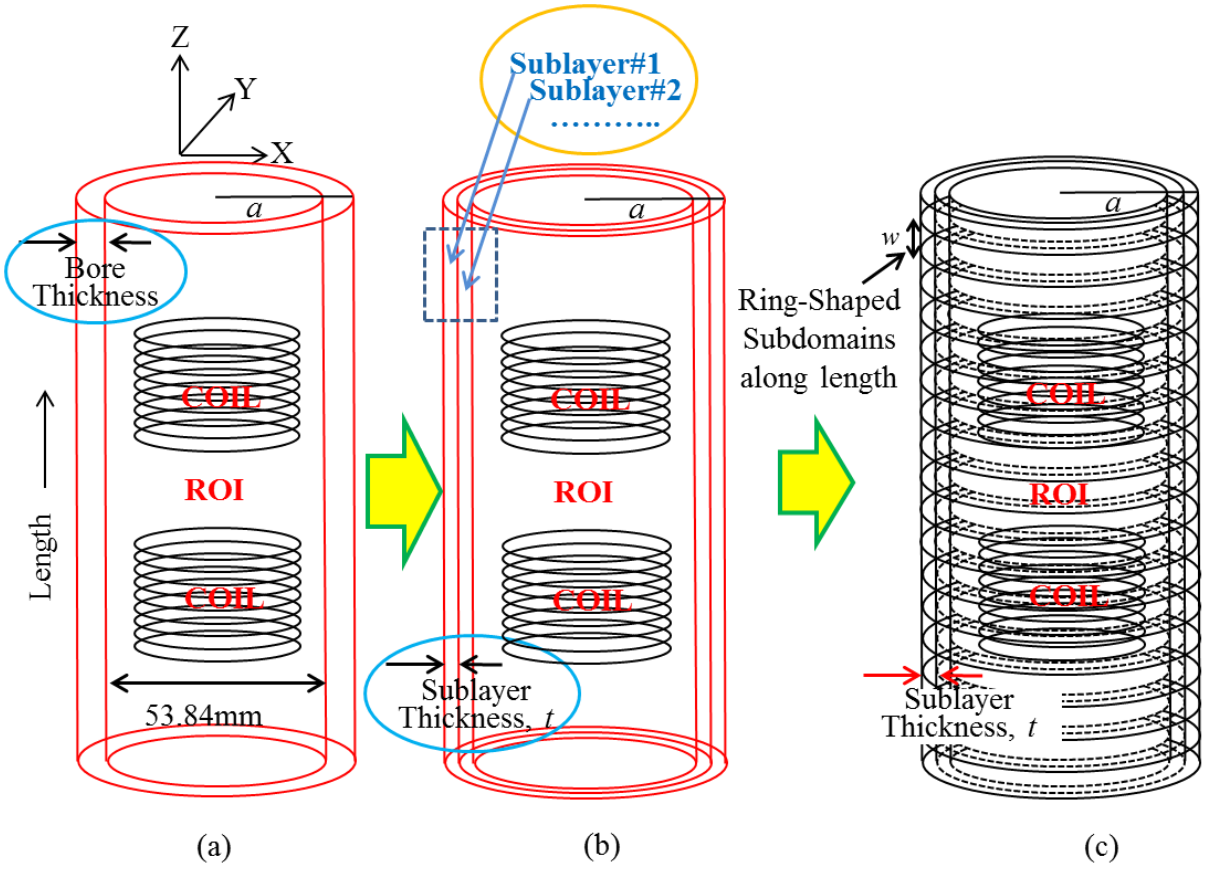

Fig. 2.11. Coupled circuit modeling for eddy current induced by cylindrical Z-gradient coil: (a) Schematic of the innermost Cu bore (diameter 53.84 mm) and cylindrical Z-gradient coil; (b) The cylindrical bore is divided into thin cylindrical sublayers along the thickness; and (c) All of the cylindrical sublayers are again divided into ring-shaped subdomains along the Z-axis.

On the other hand, to compute the inductive coupling between cylindrical Z-gradient coil and any subdomain we implemented solid angle inductance calculation approach that we have followed for planar Z-gradient coil. As the coil loops for cylindrical Z-gradient coil is circular, we implemented the same circular solid angle formula as was mentioned in the previous section for the planar Z gradient coil. The total magnetic flux enclosed by a circular ring is the inductive coupling between gradient coil and that subdomain. The calculation approach is similar to the approaches explained for planar Gz coil.

For the modeling of cylindrical Gx coil induced eddy current analysis, we considered rectangular segmentation solid angle calculation approach similar to the analysis of eddy currents induced by planar Gx coil. As the cylindrical Gx coil has 3-D curvatures considering the spherical geometry, we divide each coil loop into rectangular segments on the cylindrical surface (as is illustrated in Fig. 2.12) and calculate the inductive coupling between coil and subdomains considered in the conducting bore.

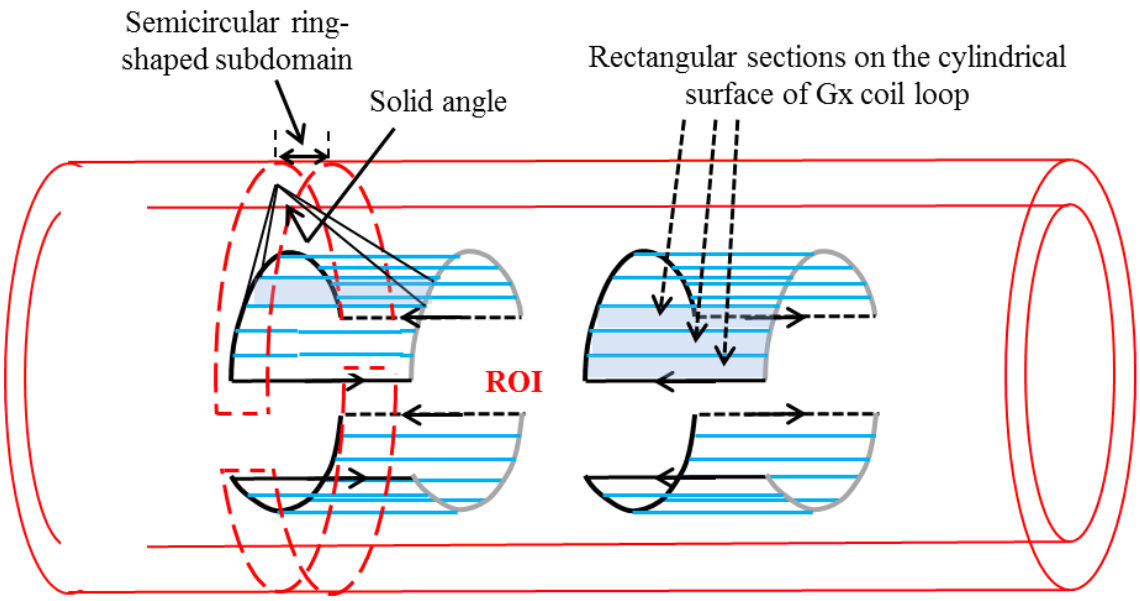

Fig. 2.12. Rectangular segmentation of X-gradient coil loops on its cylindrical surface.

The actual coil loop is shown in Fig. 2.13(a) and (b) – the coil has 12 loops in one quarter. Fig. 2.13(c) shows the rectangular segmentation of one coil loop (Loop#08) for solid angle calculation. On the other hand, since the current circulates in the upper and lower half of the gradient coil with opposite direction (as shown in Fig. 2.14(a) by a simple ideal Gx coil loop), and as the net magnetic flux enclosed by a complete circular ring-shaped subdomains (that was considered for cylindrical Gz coil analysis) is zero in case of Gx coil (Gx coil field distribution is shown in Fig. 2.14(b) by blue arrows), we considered semicircular subdomains (as is shown in Fig. 2.14(c)) for Gx coil induced eddy current simulation.

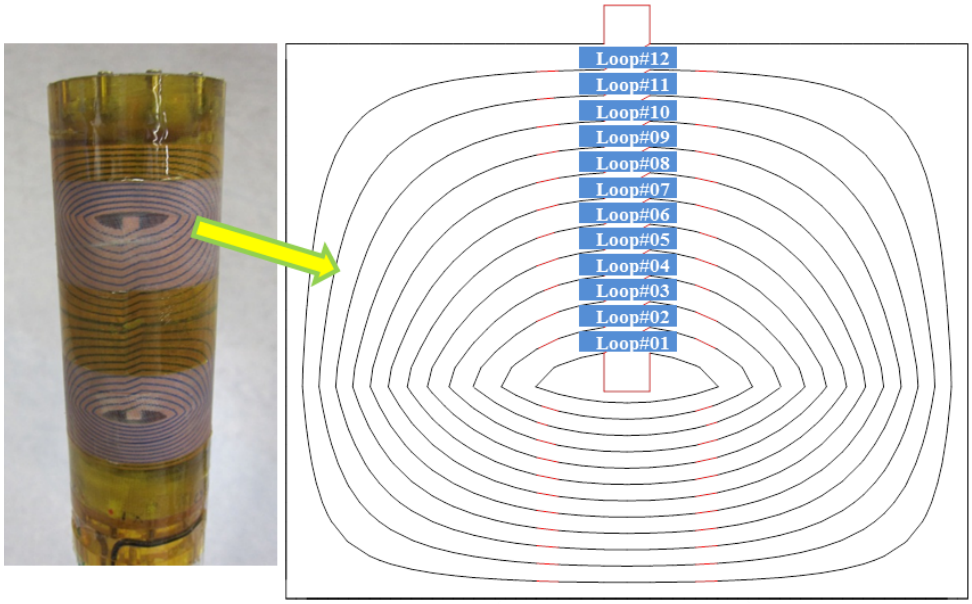

(a) (b)

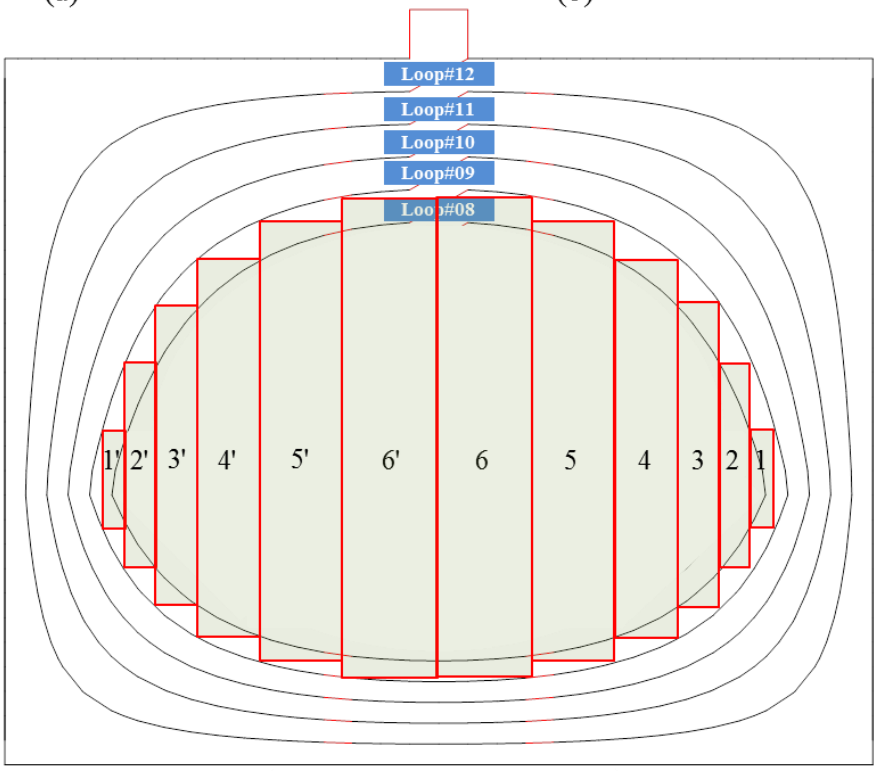

(c)

Fig. 2.13. (a) Cylindrical X-gradient coil; (b) Schematic of one quarter of cylindrical X-gradient coil with 12 loops; (c) Segmentation of the area of loop#08 into rectangular sections. Here the total area is segmented into 12 rectangular sections of which every segment (e.g., 1) on the right has a same segment (e.g., 1') on the left. Calculation of solid angle of 6 segments from left or right will be needed.

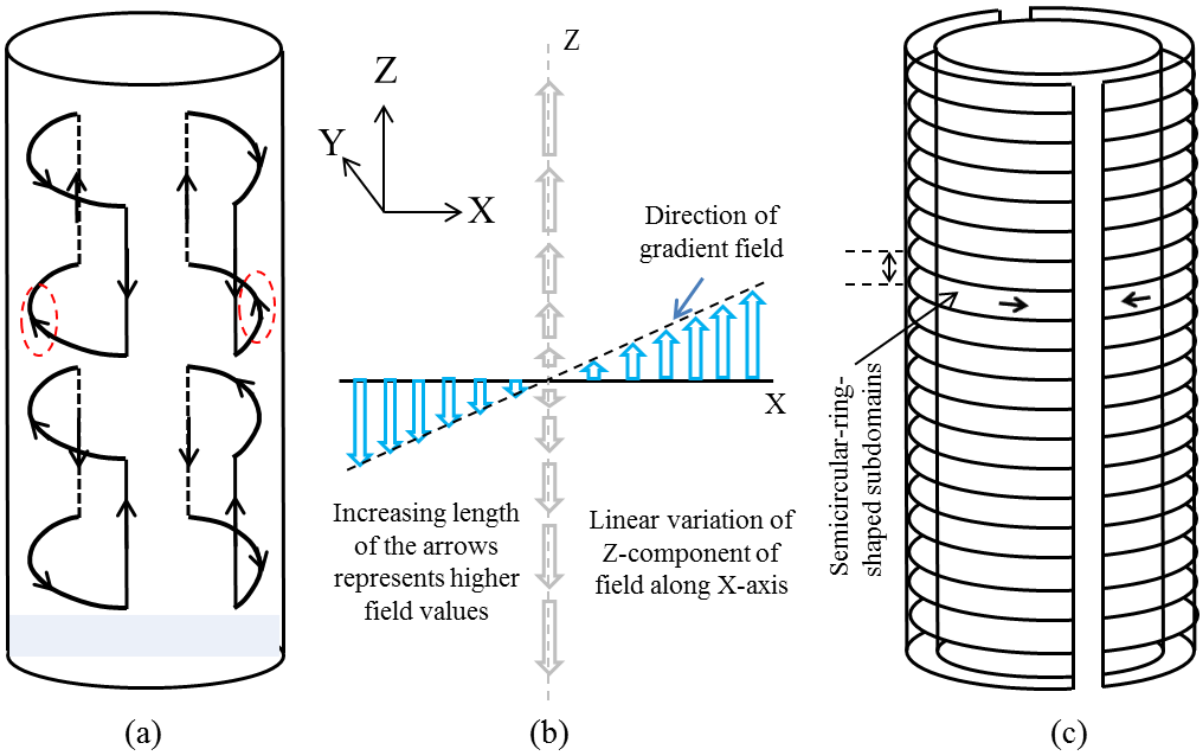

Fig. 2.14. (a) A simple Gx coil pattern to illustrate the current directions in the four set of coils; (b) Linear X-gradient field; (c) Coupled circuit modeling of cylindrical conducting bore into semicircular subdomains. Since the current in the right and left loops have currents in opposite directions (as is marked by dashed red circles in Fig 2.14(a)), the subdomains are taken as semicircular to simulate the eddy current responses.

2.5 Experimental Setup

2.5.1 0.3 T Open MRI System

We compared our simulation results for planar Z-gradient coil by implementing the single-point-like phantom experiment [2,12] to measure the time evolution of free induction decay (FID) signal for the induced eddy current phase variations [29]. We designed an NMR probe consisting of a solenoid RF coil wound around a 6 mm-diameter glass sphere filled with baby oil, tuning and matching capacitors, and a rectangular shield box made of brass plates. The internal structure of the NMR probe and the experimental setup are shown in Fig. 2.15(a).

The NMR probe was located at a given position in the region of interest (ROI) by a three-axis stepper motor stage with accuracy of 0.1 mm, and paired FID signals with opposite gradient polarity were measured followed by a 40 μs nonselective (hard) RF pulse to calculate the temporal evolution of the eddy current fields. Experimental details with the applied gradient configuration are presented in Fig. 2.15(b).

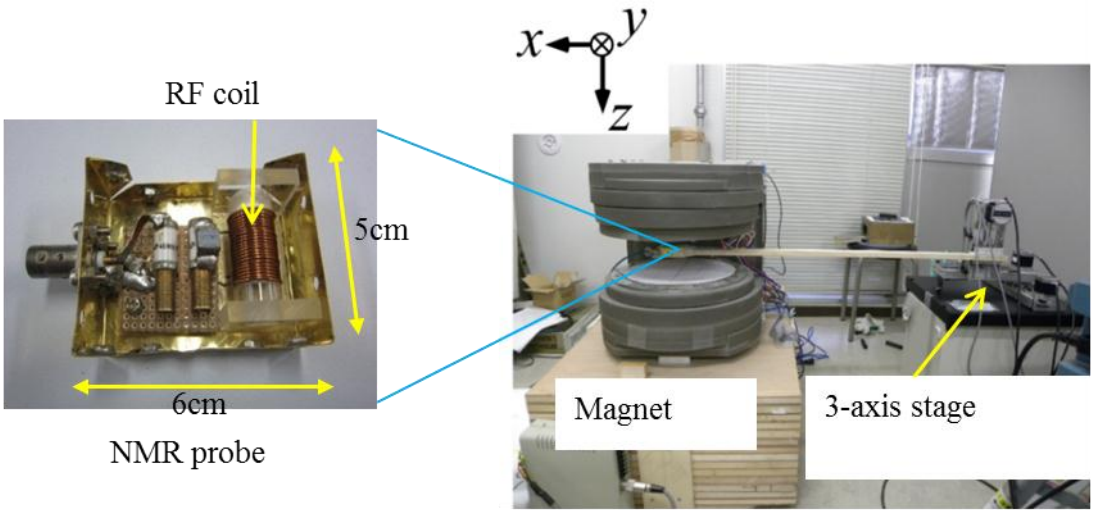

(a)

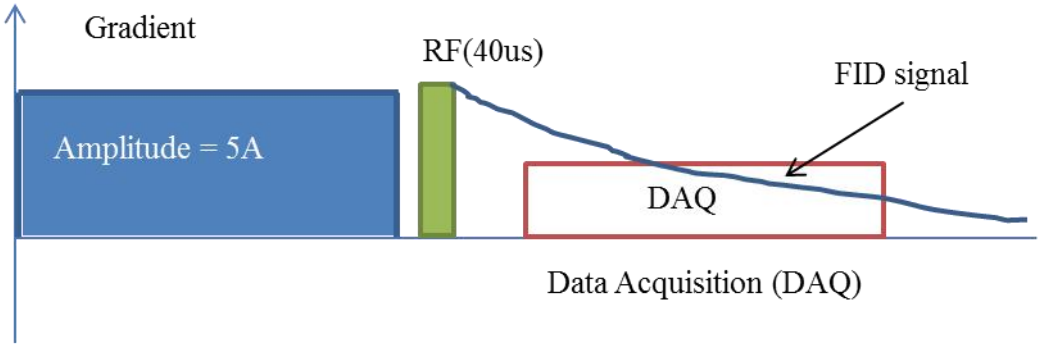

(b)

Fig. 2.15. Experimental setup to conduct FID measurements of eddy current fields. (a) The NMR probe was positioned at a given position by a three-axis stepper motor stage with accuracy of 0.1 mm. The NMR probe consisted of a solenoid RF coil wound around a 6 mm-diameter glass sphere filled with baby oil, tuning and matching capacitors, and a rectangular shield box made of brass plates. (b) Schematics of the signaling in the FID experiment. An amplitude of 5 A of the trapezoidal signal with a nominal rise and fall time of 170 μs and constant duration of 1.06 ms was used in the experiment. An RF hard pulse was applied immediately after the gradient and FID signals were measured for the opposite gradient polarity signals by the NMR probe.

2.5.2 9.4 T Closed-Bore MRI System

In case of eddy current measurement for 9.4 T superconducting magnet MRI system we implemented a gradient echo shift measurement technique [19] in which the gradient eddy currents are represented by

$$EC = \frac{m}{2\pi\gamma TE}$$

where, *m* is the slope of the phase, γ magnetogyric ratio and *TE* is the time between midpoints of the RF transmit pulse and the acquisition window (Fig. 2.16(a) [19]). This technique does not require precise positioning of the phantom (we used water phantom) at different positions and eddy current phase from a comparatively large phantom can be calculated by using a simple gradient echo sequence (as is shown in Fig. 2.16(a)). The gradient eddy currents, hence the shift of gradient echos due to eddy current generated phase accumulation are measured at various delay times (*TE*). In Fig. 2.16(b) the red marked area corresponds to the shift of echo (Δ) from its intended time-position (marked by dotted red line in Fig. 2.16(b)) because of eddy current generated phase accumulation.

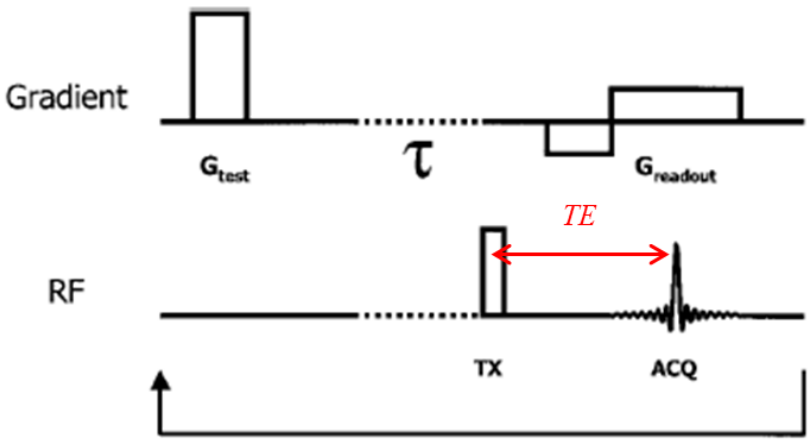

(a)

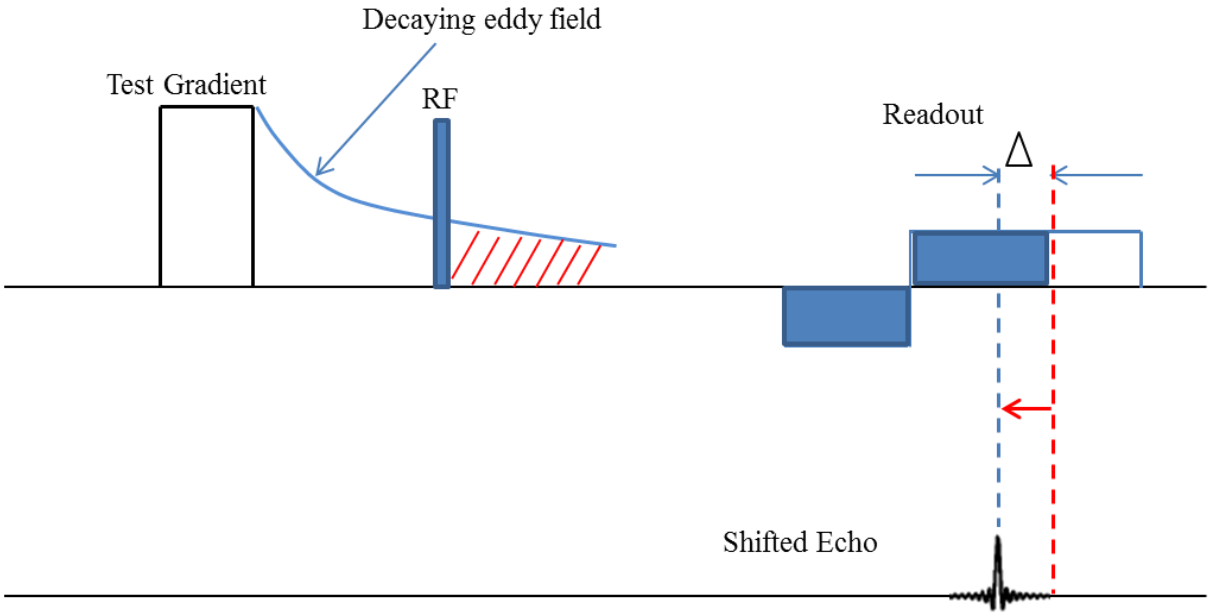

(b)

Fig. 2.16. (a) The pulse sequence implemented for the eddy current experiment in 9.4 T MRI system. (b) Illustration of echo shifting effect because of eddy current generated unwanted phase. Red marked area corresponds to the shift of echo (Δ) from its intended time-position (marked by dotted red line) because of eddy current generated phase accumulation.

Chapter 3

Results

3.1 0.3 T Open MRI System

3.1.1 Simulation Parameters

We considered the distribution of eddy currents in the local RF shielding box induced by both Z-gradient and X-gradient coils. The shielding box was positioned within the 122 mm magnet gap, symmetrical to the center of the gradient coil. The box is made of 0.3 mm-thick brass plates of resistivity ρ, $6 \times 10^{-8}\ \Omega.\mathrm{m}$, and with boundary dimensions of 220 mm×180 mm×100 mm . Both the upper and lower Z-gradient coils have similar circular loops of maximum diameter 315.42 mm consisting of 30 circular turns. On the other hand, the X-gradient coil were designed as a combination of circular arc and second-order Bezier curve with the position and center angle optimized using Genetic algorithm [51]. In each part there have 16 turns of coil and the coil pattern was restricted to a circular region of 320 mm in diameter. For both type of coils, each gradient coil element was made by winding polyethylene-coated copper wire of 0.6 mm diameter on a surface of fiber-reinforced plastic (FRP) plate. The applied gradient signal was of the trapezoidal type with a ramp-up and ramp-down time of 170 μs and flattop duration of 1.06 ms. The corresponding skin depth was 1.60739 mm.

Because the upper and lower plates of the local shielding box are in the X–Y plane, perpendicular to the Z-gradient (Gz) field direction, and the Z component (axial component) of the Gz field has a much higher value than the negligible X and Y components, the eddy currents can be assumed to exist mostly in the upper and lower plates of the shielding box. Following the coupled circuit method, we took two 0.15 mm-thick sublayers of each plate, which was considered to be sufficiently thin (less than one-tenth of the skin depth (1.60739 mm at 5.882

KHz)) to assume a constant eddy currents along the thickness (along the Z-axis). To consider the eddy current distribution along X- and Y- axis, we have again divided each sublayer into thin subdomains along each direction. In this simulation we have considered subdomains of equal width of 2 mm. In this way, subdomains taken in each layer along X-axis were 110 and along Y-axis were 90. The number of Eigen values was twice of these values for each direction as we have divided each plate into two thin sublayers. The dimension of each subdomain divided along the length of each brass plate was 180 mm×2 mm×0.15mm and along the width was 220 mm×2 mm×0.15 mm.

3.1.2 Results and discussion

The coupled network calculation was conducted using the Mathematica® programming platform in a desktop computer (Processor: Intel(R) Core(TM)2 Duo E7500 @ 2.93 GHz 2.93 GHz; OS: Windows 7 Professional; Memory (RAM): 4.00 GB). In the calculation, at first we performed the computation of the resistance matrix, $\mathbf{R}_i$, and the inductive coupling matrices, $\mathbf{M}_{ii}$, and $\mathbf{M}_{is}$. Then, we used these data in the network equation to compute eddy current responses. Once we had constructed these matrices for a given configuration of the MRI system, we could implement them in the calculation of eddy currents for any time-dependent current applied to the gradient coil.

3.1.2.1 Z-Gradient Eddy Current Response

In our analysis, we found that the amplitudes of eddy currents along the X- or Y-axis were symmetric to the center of the plate, which is expected from the positioning of the gradient coil and the upper or lower plate of the local shielding box as illustrated in Fig. 3.1(a). Fig. 3.1(b) depicts the nature of the eddy current distribution along the Y-axis of the upper plate for the

outermost sublayer. Results are given for different time instants of the decaying currents. In addition, the central subdomain was found to have the largest amplitudes.

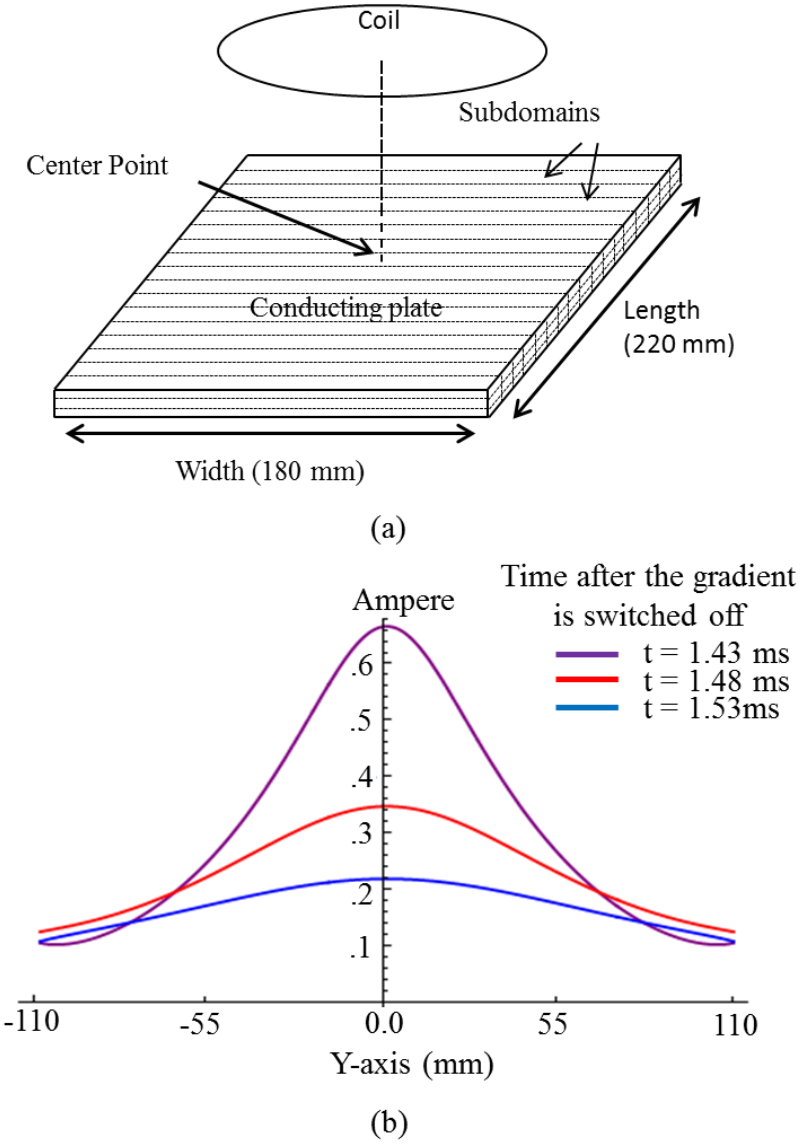

Fig. 3.1. (a) Schematic of coupled circuit modeling of one conducting plate of RF shielding box considering Z-gradient induced eddy currents. (b) Eddy Current Amplitude distribution along the length of the RF shielding box.

In Fig. 3.2, eddy current responses are given as a function of time for few subdomains located at different positions in the Y-axis. Fig. 3.2(b) presents the eddy current transients for several domains located on the negative Y-axis and Fig. 3.2(c) is for similar domains on the positive Y-axis. Here, we see that transient responses have similar characteristics on both sides

from the center of the plate. We also see that the eddy current responses during both ramp-up and ramp-down have rapid transient characteristics, whereas they show a slower exponential decay when there is no change in the input gradient signal. These characteristics are found to be in agreement with the physics of a network of inductively coupled circuits. In accordance with Lenz's law, the responses of eddy currents during the rising or falling portion of the input gradient signal clearly depict the opposing nature of eddy currents in an MRI system.

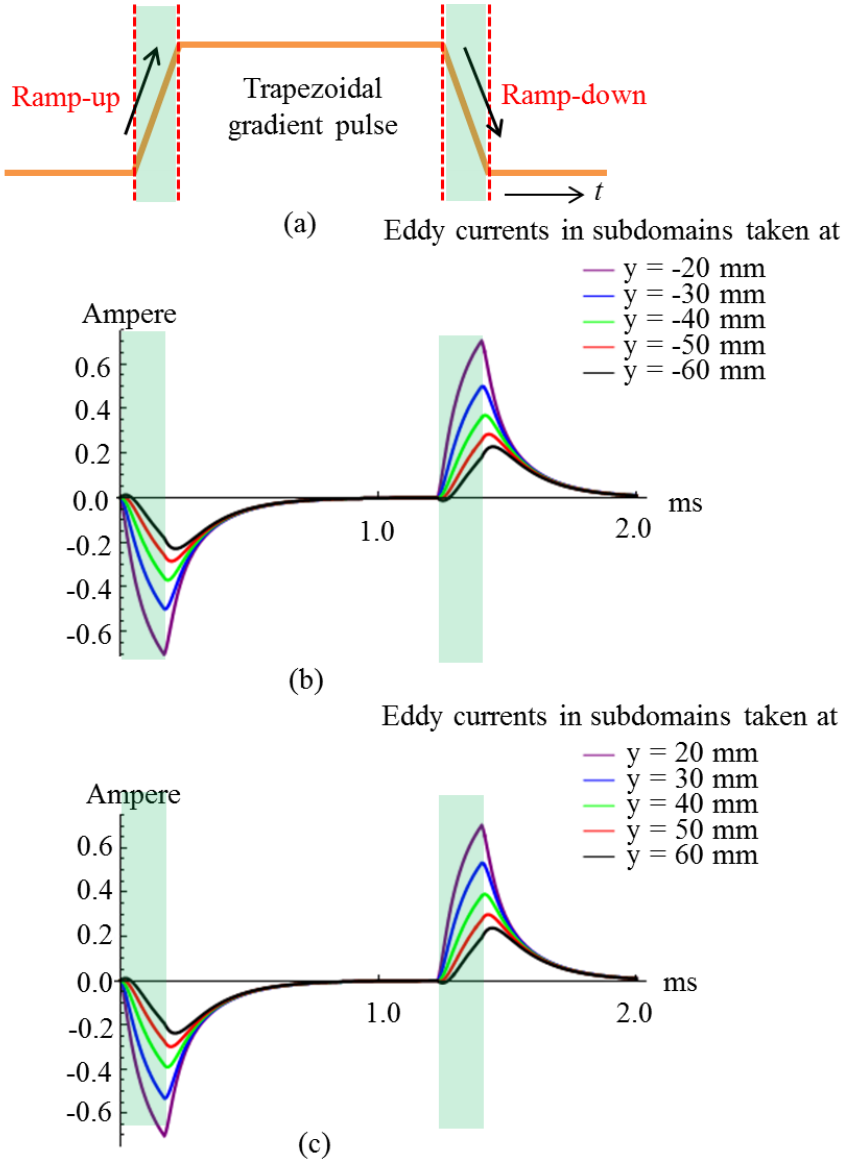

Fig. 3.2. (a) Trapezoidal Signal showing the ramp-sup and ramp-down portion – eddy currents develop during these switching; (b) and (c) Transient responses of eddy currents in different subdomains taken along the Y-axis

The secondary magnetic fields generated by these eddy currents can be determined by the Biot–Savart law. To verify the simulation results, we conducted FID measurements of the eddy current fields. In the measurements, the NMR probe was positioned at different points in the region of interest (ROI – around the center of the magnet gap), and the same procedure was repeated. We took FID signals for two cases: a) keeping the brass box inside the magnet, and b) without the brass box. The latter case was used to measure the secondary field due to other components of the MRI system. These results were then subtracted to get the secondary field generated by eddy currents in the shielding box only.

The simulation and experimental results of transient eddy current magnetic fields are combined in Fig. 3.3 (a) and (b), respectively. Results are given for several points along the Z-axis for both the positive and negative sides from the center of the region of interest (ROI). We found that similar points on either side from the axis origin (center of the magnet) have nearly the same responses with opposite polarity of field amplitudes. The time constants of the decaying transient secondary fields are listed in Fig. 3.3(c) for several points along the Z-axis. As for the experiments, each FID signal was exponentially fitted to calculate the time constants. The decaying field showed a time constant of around 170 μs. Fig. 3.4 depicts the results of the secondary field along the Z-axis for different instances of the gradient signal. The responses are nearly linear along the Z-axis. We found good agreement between the simulation and experimental results.

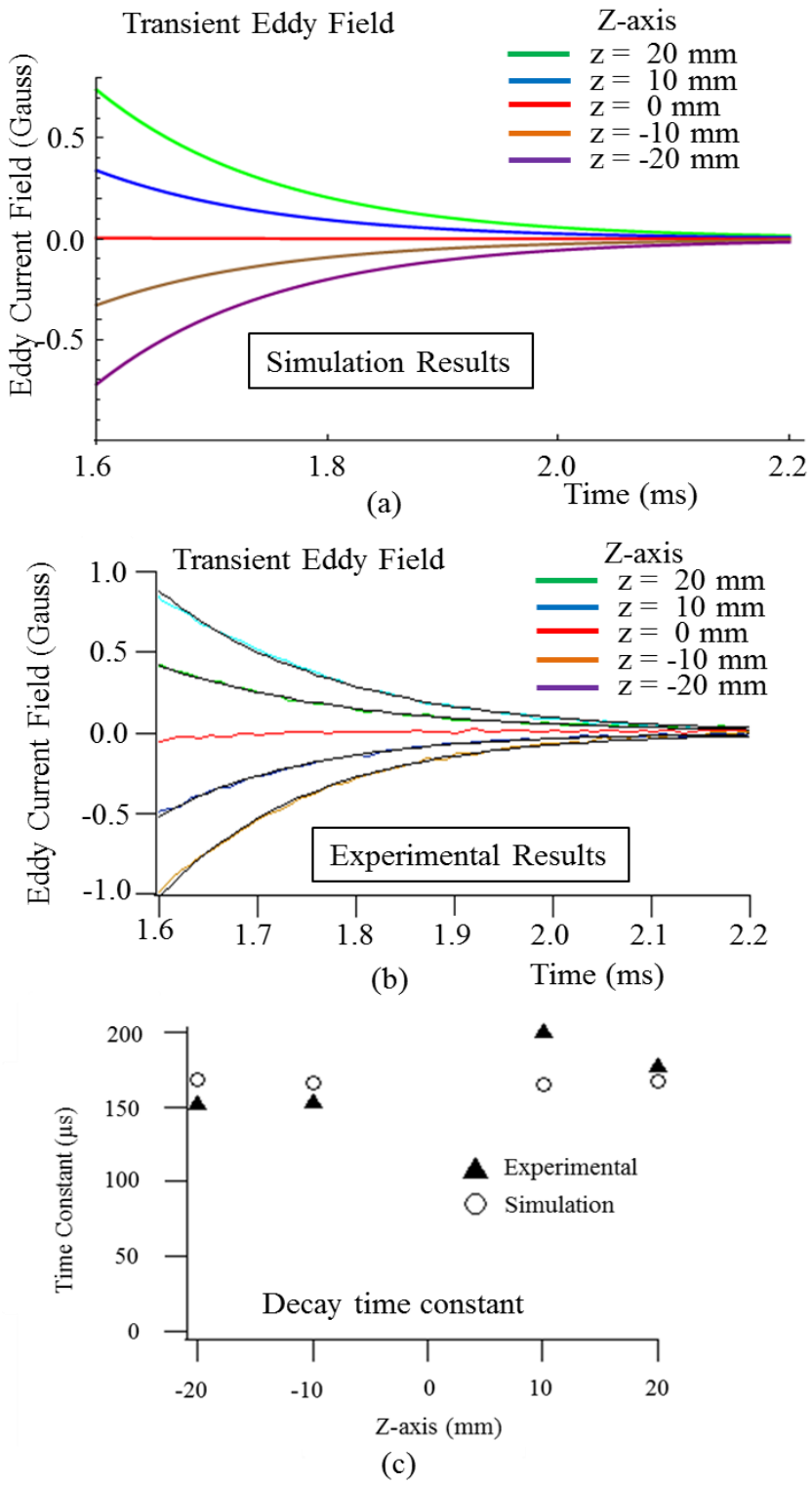

Fig. 3.3. (a) Simulation results of Z-gradient induced eddy current transient field response generated at several points along the Z-axis; (b) The experimental eddy current transient field; and (c) Comparison of eddy field time constants at several point along the Z-axis.

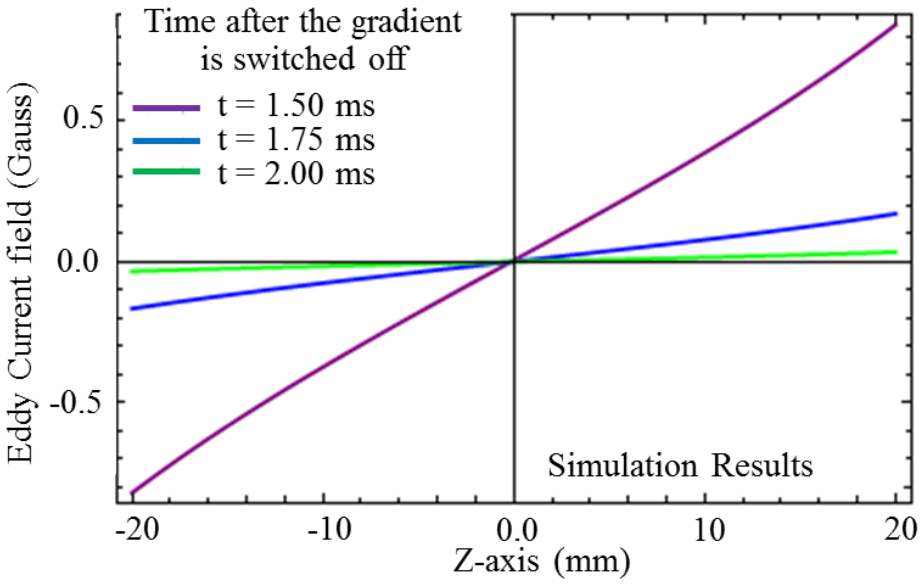

(a)

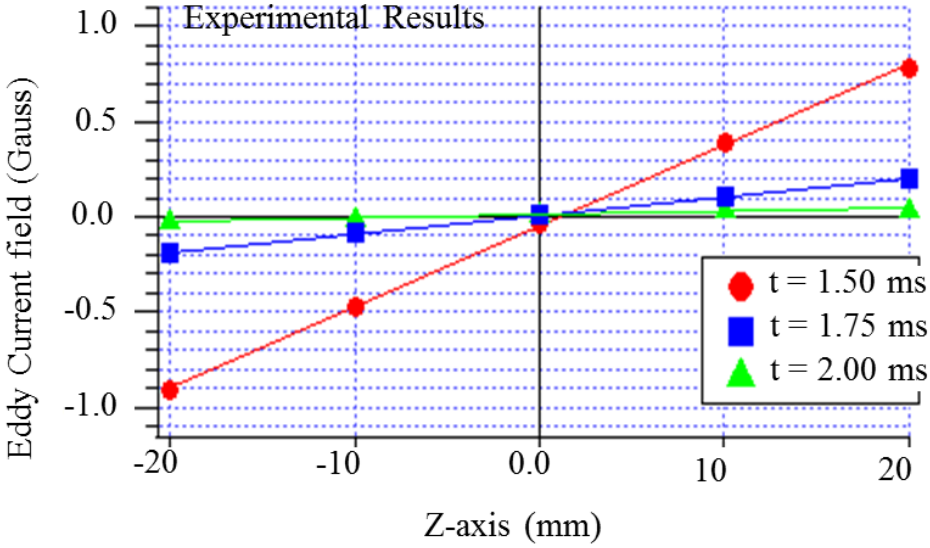

(b)

Fig. 3.4. (a) Simulation results of spatial response of eddy current field along the Z-axi- Results are given for different time instants after the gradient pulse was switched off; (b) The experimental eddy current spatial response along the Z-axis.

3.1.2.2 X-Gradient Eddy Current Response

Simulation for X-gradient induced eddy currents was conducted in the similar fashion as that for the Z-gradient coil. But the solid angle for a coil in the X-gradient set is asymmetric considering the center of the magnet and also considering the center of the spherical space bounding the coil and the ROI. For this reason we have followed a segmentation solid angle calculation approach following the calculation method given in reference [57]. Also Gx coil has four sets (two sets in the upper layer and two sets in the lower layer near the magnet poles) of coils compared to the two sets of coils for planar Z-gradient coil. For both of these reasons, more calculation resources were needed for the simulation of X-gradient coil generated eddy currents. The computational time become two times longer (approximately six minutes) than the time required for Z-gradient eddy current simulation. In Fig. 3.5(b) we have illustrated eddy current distribution along the X-axis. In accordance with the Gx coil response the eddy current response was found nearly zero at the center of the plate whereas subdomains considered at either side from the center show increasing values. Fig. 3.6(a) illustrates the transient secondary magnetic fields for few points in the ROI. Compare to the Z-gradient transient eddy field (illustration given in Fig. 3.3), X-gradient eddy field was found to decay faster with an approximate decay time constant of 70 μs. The linear eddy current field response is given in Fig. 3.6(b). Here also we see that the secondary X-gradient fields have smaller responses than the secondary Z-gradient fields (illustration given in Fig. 3.4). Since the current circulates in the opposite directions in the two sets of coil in each layer of planar X-gradient coil, they also have opposing secondary magnetic field response in the region of interest (ROI).

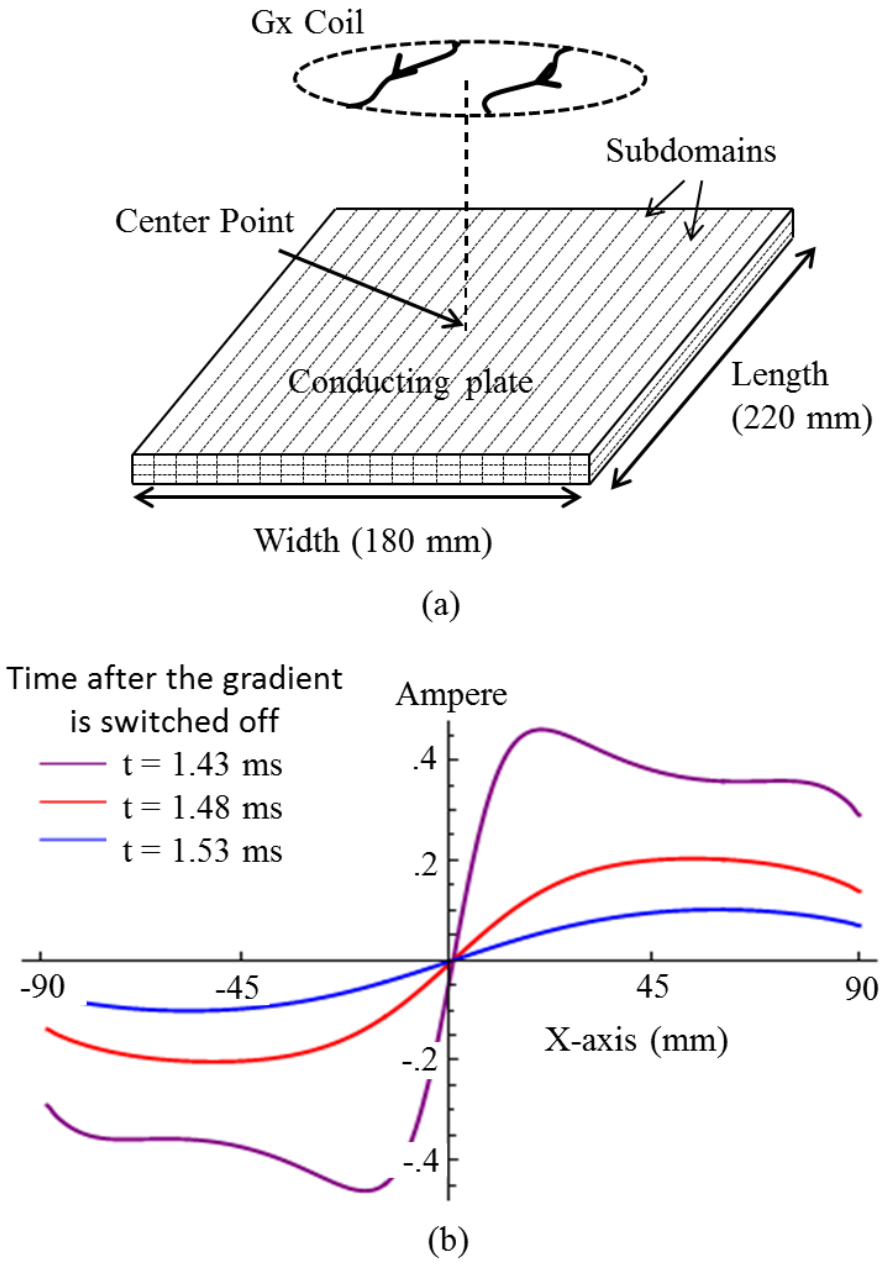

Fig. 3.5. (a) Schematic of coupled circuit modeling of one conducting plate of RF shielding box considering X-gradient induced eddy currents. (b) Eddy Current Amplitude distribution along the width (X-axis) of RF shielding box.

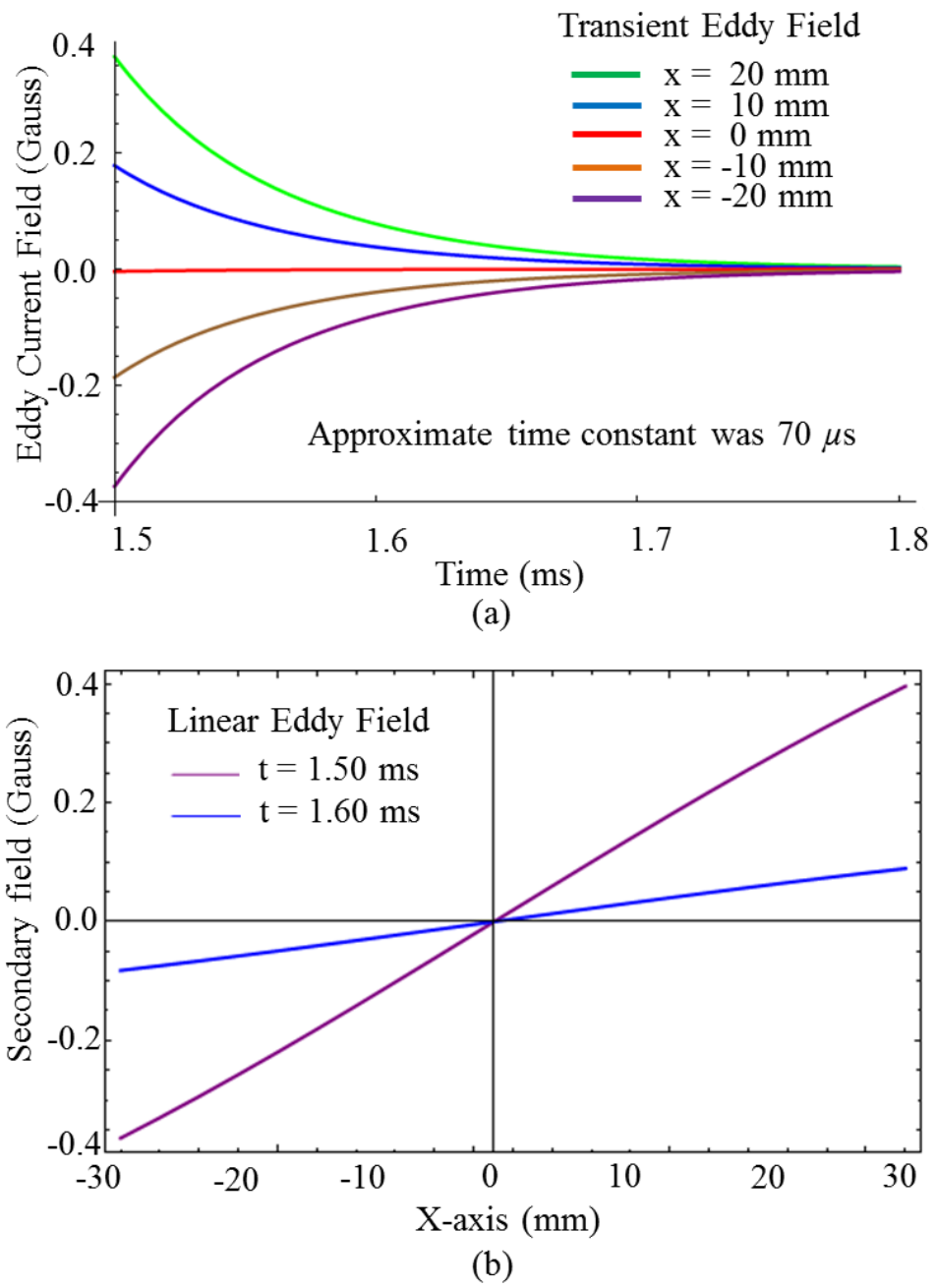

Fig. 3.6. (a) Transient eddy field generated by the eddy current induced by the X-gradient coil. (b) Eddy field spatial response along the X-axis.

3.2 9.4 T Closed-Bore MRI System

3.2.1 Simulation Parameters

The superconducting magnet is of vertical type and consisted of several cylindrical conducting bores in its cryostat structure (shown in Fig 2.10) of which the innermost layer is the warm bore (298 K) and the other three cold shields are the second bore (77 K), third bore (4.2 K) and fourth bore (4.2 K). Details of the properties are again given in Table 2. In this study, the gradient test pulse we considered is a trapezoidal pulse with ramp-up and ramp-down time of approximately 200 μs and large flattop duration of 50 ms to avoid the superposition of eddy currents generated during the ramp-up portion of the signal. The corresponding calculated skin depth was 1.01399 mm. As the thickness of subdomains ideally should be infinitely thin [37], to consider the fast switching effect of the gradient pulse we divided the cylindrical bore into thin cylindrical sublayers of thickness 1/10th of the skin depth as it was taken for the simulation of eddy currents in case of 0.3 T open MRI system. The 1.63 mm thick copper innermost bore (resistivity 2.0284×10^{-8} Ω.m) were divided along the thickness (along the radial direction) into 16 cylindrical sublayers of thickness 0.101399 mm each. Each sublayer is again divided into 2 mm width 200 circular ring subdomains along the length (Z-axis) of the cylinder – we considered the central 400 mm region (2 mm × 200 subdomains) to analyze the eddy current response. In our study we found the eddy current amplitude beyond this region is negligible.

Table 2 Dimensions and material properties of superconducting magnet bores

Bore #	Materials	Diameter (mm)	Thickness (mm)	Temperature	Temperature Coefficient (/K)	Resistivity, ρ (Ω-m)
1st Bore	Cu (C1220)	53.84	1.63	293 K	.0039	$2.0284X10^{-8}$
2nd Bore	Cu (C1220)	61.14	1.63	77 K	.0039	$1.1009X10^{-8}$
3rd Bore	Cu (C1220)	69.74	1.63	4.2 K	.0039	$0.9545X10^{-8}$
4th Bore	Al (AC4C)	81.1	3.00	4.2 K	.0043	$1.9273X10^{-8}$

In case of X-gradient coil coupled circuit modeling, we considered semicircular subdomains instead of complete circular subdomains since the net flux enclosed by a circular ring subdomain is zero for Gx cylindrical coil (as we explained in the Methods and Material chapter (section 2.4, Fig. 2.14)). At first we divide the vertical cylindrical bore vertically into two half cylinders as is illustrated in Fig. 2.14(c). Similar to previous modeling approaches we considered the thickness cylindrical sublayers to be 1/10th of the skin depth and width of each semicircular subdomain was 2 mm. The total number of sublayers considered in each half-cylindrical bore was 16 for the innermost bore and subdomains in each sublayer were 200 considering the central 400 mm region that we also considered for cylindrical Gz coil. The simulation parameters for the inner four conducting bores considering both the Z- and X-gradient coils are listed in Table 3.

Table 3 Simulation parameters for cylindrical Gz and Gx coils

Bore #	Sublayer thickness (mm)	No of Sublayers	Subdomain width (mm)	Subdomains/sub layer
1st Bore	0.1014	16	2	200
2nd Bore	0.0747	21	2	200
3rd Bore	0.0695	23	2	200
4th Bore	0.0987	30	2	200

3.2.2 Results and discussion

Simulations were conducted for eddy currents in the inner four bores generated by Gz and Gx coils. Table 4 summarizes the amplitudes and time constants of eddy field separately generated by the eddy currents in each bore considering both the Z- and X-gradient coils. Results for the simulated gradient eddy current field generated by the induced eddy currents in the inner four bores of the superconducting magnet are given in Fig. 3.7 (a) and (b) respectively for Z- and X-gradient coils. We have performed gradient echo shift measurement of gradient eddy field in

the imaging region of 5 mm diameter sphere at the center of the magnet. Table 5 summarizes and compares the simulation and experimental results of the eddy current parameters for both Z-gradient coil and X-gradient coils. In the measurement results we got two time constants (1 ms and 10 ms (approximately)) with considerable amplitudes of the gradient eddy fields. The simulation results considering eddy currents in the inner four bores matches with the faster component. For the slower component a complete simulation considering the superconducting wire, conducting bores and all of the gradient coils would be needed.

Table 4 Simulated eddy current field parameters

Gradient coil	Parameters	Innermost bore (298 K)	Second bore (77 K)	Third bore (4.2 K)	Fourth bore (4.2 K)
Gz coil	Amplitude (G/cm)	0.2989	0.2180	0.1565	0.1022
	Time constant (ms)	1.04	1.94	2.28	1.27
Gx coil	Amplitude (G/cm)	0.3034	0.1750	0.1367	0.1013
	Time constant (ms)	1.06	1.80	2.43	1.63

Table 5 Comparison of simulated and experimental results for cylindrical coils

Results	Z-gradient Coil		X-gradient Coil	
	Amplitude (G/cm)	Time constant (ms)	Amplitude (G/cm)	Time constant (ms)
Simulation results	0.7757	1.48	0.7166	1.50
Experimental results	0.76±0.05	0.93±0.06	0.67±0.03	1.02±0.07

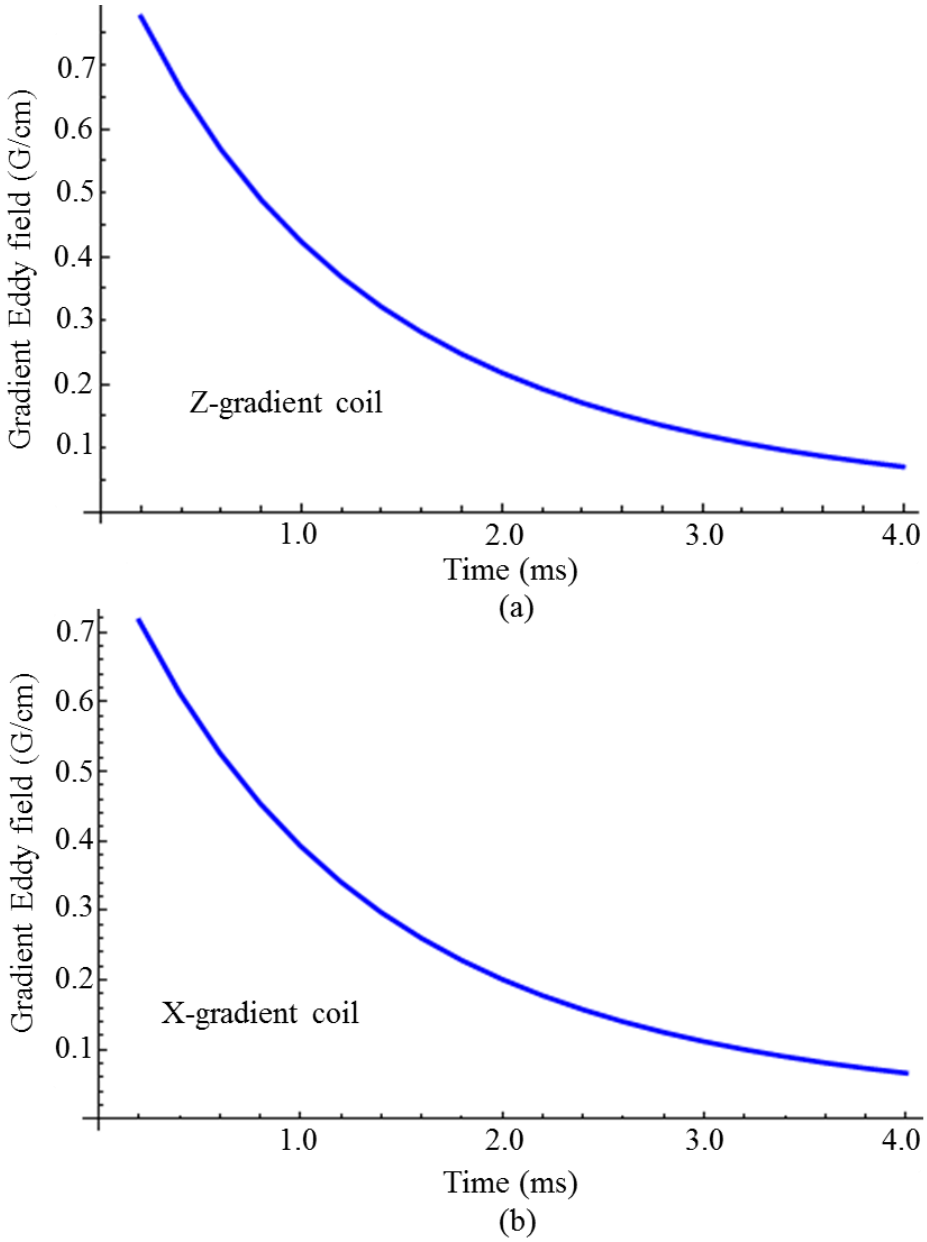

Fig. 3.7. Simulated transient gradient eddy current field for the eddy current induced by the (a) Z-gradient coil and (b) X-gradient coil.

Chapter 4

Conclusion

In this study we conducted coupled circuit simulation of eddy currents in both open MRI (induced by planar type gradient coils) and closed-bore MRI (induced by cylindrical type gradient coils) systems by implementing novel approaches. For coupled circuit modeling of the eddy current conducting structures we considered bar-shaped subdomains considering eddy currents induced by both longitudinal (Gz) and transverse (Gx or Gy) planar gradient coils, circular ring-shaped subdomains for cylindrical longitudinal (Gz) gradient coil, and semicircular subdomains for cylindrical transverse (Gx or Gy) gradient coils. In all of these cases the thickness and width of each subdomain were considered as 1/10th of the skin depth and 2 mm, respectively. To compute the inductive coupling between gradient coil and subdomain at any position solid angle form of Ampere's law was implemented. For both planar and cylindrical type longitudinal (Gz) gradient coils circular loop solid angle formula for 3-D was calculated considering the coil loops as separate circles. In case of transverse (Gx or Gy) gradient coils of both planar and cylindrical types, as the coil loops have irregular geometrical shapes and asymmetry considering the center of the coil, we suggested a rectangular segmentation solid angle calculation approach in which the coil loop area is divided into several rectangular sections and simple rectangular solid angle formula was implemented to calculate the total solid angle. The system of first-order differential equations formulated from the network of resistive-inductive circuits (that represents all of the subdomains and gradient coils) was solved by implementing Eigen method solution approaches. As the system of equations possesses both homogeneous and nonhomogeneous differential equation formats we solved the homogeneous problem by implementing decoupling solution method and nonhomogeneous problem by using

fundamental matrix method. The whole simulation was conducted in a general purpose desktop PC with 4 GB memory (RAM). To verify our simulation results we conducted single point-like phantom FID experiment for open MRI system and gradient echo-shift measurement experiment for closed-bore MRI system. In case of open MRI system we have found very good agreement between simulation and experiment. On the other hand, the measurement results for closed-bore superconducting magnet MRI system shows multiple (at least 2) amplitudes and time constants of the gradient eddy current fields. As the superconducting magnet has multiple cold shield (77 K and 4.2 K) cylindrical bores in its cryostat structure and as the superconductor wire contain thick copper coverings, eddy currents with large time constants can generate in the superconducting magnet MRI systems. We conducted simulation for the inner four cylindrical bores (warm bore (298K), 77 K. 4.2 K, 4.2 K) for the eddy current field induced by Gz coil and Gx coil separately. The simulation results match to the fast (approximately 1 ms) decaying gradient eddy current fields. A complete calculation of eddy currents considering the superconducting coils and inductive couplings among the conducting structures might provide the slower decaying components (approximately 10 ms) of the gradient eddy current fields.

Appendix A

Publications

Journal Paper

1. **Md Shahadat Hossain Akram**, Yasuhiko Terada, Keiichiro Ishi, Katsumi Kose, Coupled Circuit Numerical Analysis of Eddy Current in an Open MRI System, Journal of Magnetic Resonance, Vol. 245, , Pages 1 – 11, August 2014.

Conference Abstracts

1. **Md Shahadat Hossain Akram**, Koki Matsuzawa, Yasuhiko Terada, Katsumi Kose, Novel Approaches in the Coupled Circuit Analysis of Eddy Current Induced by Cylindrical Gradient Coils, The International Society for Magnetic Resonance in Medicine (ISMRM) 23rd Annual Meeting and Exhibition, Ontario, Canada, 30 May – 05 June, 2015.
2. **Md Shahadat Hossain Akram**, Yasuhiko Terada, Katsumi Kose, Coupled Circuit Simulation of Z- and X-Gradient Eddy Currents in a 9.4T Narrow-Bore MRI System, The 42nd Japanese Society for Magnetic Resonance in Medicine (JSMRM), Kyoto, Japan (To be held), 18 – 20 September, 2014.
3. **Md Shahadat Hossain Akram**, Yasuhiko Terada, Katsumi Kose, Temporal-Spatial Responses of Planar X-Gradient Eddy Currents by Solid Angle Coupled Circuit Method, The 42nd Japanese Society for Magnetic Resonance in Medicine (JSMRM), Kyoto, Japan (To be held), 18 – 20 September, 2014.
4. **Md Shahadat Hossain Akram**, Yasuhiko Terada, Keiichiro Ishi, Katsumi Kose, Eigen Matrix Approach in Coupled-Circuit Numerical Simulation of Eddy Currents in MRI

Systems, Joint Annual Meeting of The International Society for Magnetic Resonance in Medicine - European Society for Magnetic Resonance in Medicine and Biology (ISMRM-ESMRMB), Milan, Italy, 10 – 16 May, 2014.

5. **Md Shahadat Hossain Akram**, Yasuhiko Terada, Keiichiro Ishi, Katsumi Kose, Eddy Current Analysis of 0.3 T Permanent Magnet MRI Systems with Planar Z-Gradient Coil, The 41st Japanese Society for Magnetic Resonance in Medicine (JSMRM), Tokushima, Japan, 19 – 21 September, 2013.
6. **Md Shahadat Hossain Akram**, Katsumi Kose, A Novel Approach in the Network Analysis of Eddy Current Induced by Planar Z-Gradient Coil, The International Society for Magnetic Resonance in Medicine (ISMRM) 21st Annual Meeting and Exhibition, Salt Lake, USA, 20 – 26 April, 2013.

References

[1] Z. P. Liang, P. C. Lauterbur, *Principles of Magnetic Resonance Imaging*, IEEE Press, 2000.

[2] M.A. Bernstein, K.F. King, X.J. Zhou, *Handbook of MRI pulse sequences*, Elsevier Academic Press, 2004.

[3] R. Plonsey, R.E. Collin, *Principles and applications of electromagnetic fields*, McGraw-Hill Book Company, Inc., 1961, page 274.

[4] H.S. Lopez, M. Poole, S. Crozier, Eddy current simulation in thick cylinders of finite length induced by coils of arbitrary geometry, J. Magn. Reson. 207 (2010) 251 – 261.

[5] Y. Iwasa, J. Bascuñán, S. Hahn, M. Tomita, and W. Yao, High-Temperature Superconducting Magnets for NMR and MRI: R&D Activities at the MIT Francis Bitter Magnet Laboratory, IEEE Trans. Appl. Superc., 20 (2010) 718 – 721.

[6] W. A. Edelstein, R. A. Hedeen, R. P. Mallozzi, S. A. El-Hamamsy, R. A. Ackermann, and, T. J. Havens, Making MRI quieter, Magn. Reson. Imag., vol. 20, pp. 155 – 163, 2002.

[7] W. A. Edelstein, T. K. Kidane, V. Taracila, T. N. Baig, T. P. Yagan, Y.-C.N. Cheng, R.W. Brown, J. A. Mallick, Active-passive gradient shielding for MRI acoustic noise reduction, Magn. Reson. Med., 53 (2005) 1013 – 1017.

[8] Q. Liu, D. G. Hughes, P. S. Allen, Quantitative characterization of the eddy current fields in a 40-cm bore superconducting magnet, Magn. Reson. Med. 31 (1994) 73 – 76.

[9] A. Trakic, F. Liu, H. S. Lopez, H. Wang, S. Crozier, Longitudinal gradient coil optimization in the presence of transient eddy currents, Magn. Reson. Med., 57 (2007) 1119 – 1130.

[10] H. S. Lopez, F. Freschi, A. Trakic, E. Smith, J. Herbert, M. Fuentes, S. Wilson, L. Liu, M. Repetto, S. Crozier, Multilayer integral method for simulation of eddy currents in thin volumes of arbitrary geometry produced by MRI gradient coils, Magn. Reson. Med. 71, 5 (2014) 1912 – 1922.

[11] R. M. Henkelman, M. J. Bronskill, Artifacts in magnetic resonance imaging, Rev. Magn. Reson. Med. 2 (1987) 1 – 126.

[12] W. M. Spees, N. Buhl, P. Sun, J. J. H. Ackerman, J. J. Neil, J. R. Garbow, Quantification and compensation of eddy-current-induced magnetic-field gradients, , J. Magn. Reson. 212 (2011) 116 – 123.

[13] P. Jezzard, A. S. Barnett, C. Pierpaoli, Characterization of and correction for eddy current artifacts for echo planar diffusion imaging, Magn. Reson. Med., 39 (1998) 801 – 812.

[14] B. J. Peng, Y. Wu, S. R. Cherry, J. H. Walton, New Shielding configurations for a simulataneous PET/MRI scanner at 7T, J. Magn. Reson. 239 (2014) 50 – 56.

[15] T. Onodero, S. Matsui, k. Sekihara, H. Kohno, A method of measuring field-gradient modulation shapes. Application of high-speed NMR spectroscopic imaging, J. Phys. E: Sci. Instrum. 20 (1987) 416 – 419.

[16] J.J. Van Vaals, A.H. Bergman, Optimization of eddy current compensation, J. Magn. Reson. 90 (1990) 52 – 70.

[17] P. Jehenson, M. Westphal, N. Schuff, Analytical method for the compensation of eddy current-effects by pulsed magnetic field gradients in NMR systems, J. Magn. Reson. 90 (1990) 264 – 278.

[18] M. Tersptra, P. M. Andersen, R. Gruetter, Localized eddy current compensation using quantitative field mapping, J. Magn. Reson. 131 (1998) 139 – 143.

[19] V. J. Schmithorst, B. J. Dardzinski, Automatic gradient preemphasis adjustment: a 15 minute journey to improved diffusion-weighted echo-planar imaging, Magn. Reson. Med., 47 (2002) 208 – 212.

[20] H. Han, R. MacGregor, B. Balcom, Pure phase encode magnetic field gradient monitor, J. Magn. Reson. 201 (2009) 212–217.

[21] H. Han, A. Ouriadov, E. Fordham, B. Balcom, Direct measurement of magnetic field gradient waveforms, Concepts Magn. Reson. Part A 36 (2010) 349–360.

[22] M.J. Sablik, R.E. Beissner, A. Choy, An alternative numerical approach for computing eddy currents: case of the double-layered plate, IEEE Trans. Mag. 20 (1984) 500 – 506.

[23] T. Takahashi, Numerical Analysis of eddy current problems involving z gradient coils in superconducting MRI magnets, IEEE Trans. Mag. 26 (1990) 893 – 896.

[24] M. Schinnerl, J. Schoberl, M. Kaltenbacher, R. Lerch, Multigrid methods for the three-dimensional simulation of nonlinear magnetomechanical systems, IEEE Trans Magnetics, 38 (2002) 1497 -1511.

[25] M. Rausch, M. Gebhardt, M. Kaltenbacher, H. Landes, (2003) "Magnetomechanical field computations of a clinical magnetic resonance imaging (MRI) scanner", COMPEL - The international journal for computation and mathematics in electrical and electronic engineering, Vol. 22 Iss: 3, pp.576 – 588

[26] B. Weiss, O. Bíró, (2003) "Multigrid for transient 3D eddy current analysis", COMPEL - The international journal for computation and mathematics in electrical and electronic engineering, Vol. 22 Iss: 3, pp.779 – 788

[27] M. U. Nabi, S. V. Kulkarni, V. R. Sule, Novel Modeling and solution approach for repeated finite-element analysis of eddy-current systems, IEEE Trans Magnetics, 40 (2004) 21 -28.

[28] M. J. Choi, I. H. Park, Transient analysis of magnetodynamic systems using Fourier transform and frequency sensitivity, IEEE Trans Magnetics, 35 (1999) 1155 -1158.

[29] X. Li, L. Xia, W. Chen, F. Liu, S. Crozier, D. Xie, Finite element analysis of gradient z-coil induced eddy currents in a permanent MRI magnet, J. Magn. Reson. 208 (2011) 148 – 155.

[30] X. Li, L. Xia, W. Chen, F. Liu, S. Crozier, D. Xie, Characterization and reduction of X-gradient induced eddy currents in NdFeB magnetic resonance imaging magnet – 3D finite

element method-based numerical studies, Conc. Magn. Reson. Part B: Magn. Reson. Eng. 39B (2011) 47 – 58.

[31] D. Zheng, Three-dimensional eddy current analysis by the boundary element method, IEEE Trans. Magn., 33 (1997) 1354 – 1357.

[32] A. Trakic, H. Wang, F. Liu, H. Sanchez-Lopez, S. Crozier, Analysis of transient eddy currents in MRI using a cylindrical FDTD method, IEEE Trans. Appl. Supercond. 16 (2006) 1924 – 1936.

[33] A. Taflove, Computational electromagnetics – the finite-difference time-domain method, London: Artech; 1995.

[34] J. B. Schneider, Planes waves in FDTD simulations and a nearly perfect total-field/scattered field boundary, IEEE Trans. Anten. Prop. 52 (2004) 3280 – 3287.

[35] I. J. Chi, F. Liu, E. Weber, Y. Li, GPU-accelerated FDTD modeling of radio-frequency field-tissue interactions in high-field MRI, IEEE Trans Biom. Engi., 58 (2011) 1789 -1796.

[36] T. Weiland, Time domain electromagnetic field computation with finite difference methods, Int. J. Num. Model. : Elec. Net. Dev. Fields 9 (1996) 296 – 319.

[37] F. Liu, S. Crozier, An FDTD model for calculation of gradient-induced eddy currents in MRI system, IEEE Trans. Magn. 42 (2006) 3854 – 3860.

[38] E. E. Kreizis, J. A. Tegopoulos, *Eddy currentsin linear conducting media*, New York: Elsevier, 1985.

[39] C. V. Dodd and W. E. Deeds, Analytical Solutions to Eddy Current Probe Coil Problems, J Appl. Phys. 39 (1968) 2829 – 2838.

[40] H. Mitsuo, M. Takeshi, H. Masashi, Three-dimensional finite element eddy current analysis by using high-order vector elements, Electr. Eng. Jpn., 147 (2004), pp. 60–67.

[41] D.X. Xie, O.A. Mohammed, G.F. Ule, C.S. Koh, *T–Ω* finite element analysis of 3D nonlinear transient eddy current problems, Adv. Comput. Des. Tech. Appl. Electromagn. Syst. (1995), pp. 211–214.

[42] O. Biro, K. Preis, On the use of the magnetic vector potential in the finite element analysis of 3-D eddy current, IEEE Trans. Magn., 25 (1989), pp. 3145–3159.

[43] O. Biro, K. Preis, An edge finite element eddy current formulation using a reduced magnetic and a current vector potential, IEEE Trans. Magn., 36 (2000), pp. 3128–3130.

[44] J.S. Weiss, Calculation of eddy currents in terms of H on hexahedra, IEEE Trans. Magn., 21 (1985), pp. 2239–2241

[45] O.A. Mohammed, F.G. Uler, A state space approach and formulation for the solution of nonlinear 3-D transient eddy current problems, IEEE Trans. Magn., 28 (1992), pp. 1111–1114.

[46] T. K. Kidane, T. P. Eagan, Y. C. N. Cheng, V. Taracila, T. N. Baig, W. A. Edelstein, R. W. Brown, Resistance effects on eddy currents in conducting cryogenic warm bore cylinder, ISMRM Twelfth Scientific Meeting, Kyoto, Japan, 2004, p. 105.

[47] M. Poole, H.S. Lopez, O. Ozaki, H. Kitaguchi, I. Nakajima, S. Urayama, K. Sato, H. Fukuyama, S. Crozier, Simulation of gradient coil induced eddy currents and their effects in a head-only HTS MRI magnet, IEEE Trans. App. Super. 21 (2011) 3592 – 3598.

[48] T.K. Kidane, W.A. Edelstein, T.P. Eagan, V. Taracila, T.N. Baig, Y.-C.N. Cheng, R.W. Brown, Active-passive shielding for mri acoustic noise reduction: network analysis, IEEE Trans. Mag. 42 (2006) 3854 – 3860.

[49] W. Peterson, The fixed point method approach to nonlinear open boundary eddy current problems under TM field excitation, Magn. Reson. Med. 57 (2007) 1119 – 1130.

[50] Jianming Jin, *Analysis and design in magnetic resonance imaging*, CRC Press, 1999.

[51] Y. Terada, S. Kono, D. Tamada, T. Uchiumi, K. Kose, R. Miyagi, E. Yamabe, H. Yoshioka, Skeletal age assessment in children using an open compact mri system, Magn. Reson. Med. 69 (2013) 1697 – 1702.

[52] S. Handa, T. Haishi, K. Kose, Development of a local electromagnetic shielding for an extremity magnetic resonance imaging system, Rev. Sci. Ins. 79 (2008) 113706-1 – 3.

[53] F. Paxton, Solid Angle Calculation for a Circular Disk, Rev. Sci. Inst. 30 (1959) 254 – 258.

[54] H. M. Haitjema, Evaluating solid angles using contour integrals, Appl. Math. Mod. 11 (1987) 69 – 71.

[55] E. Galiano, C. Pagnutti, An analytical solution for the solid angle subtended by a circular detector for a symmetrically positioned linear source, Appl. Rad. Isot. 64 (2006) 603 – 607.

[56] S. Pomme, L. Johansson, G. Sibbens, B. Denecke, An algorithm for the solid angle calculation applied in alpha-particle counting, Nucl. Inst. Meth. Phys. Res. A 505 (2003) 286 – 289.

[57] H. Gotoh, H. Yagi, Solid angle subtended by a rectangular slit, Nucl. Inst. Meth. 96 (1971) 485 – 486.

[58] W.T. Scott, *The physics of electricity and magnetism*, 2nd Edition, John Wiley& Sons, Inc., Tokyo, 1959.

[59] J. D. Jackson, *Classical electrodynamics*, 3rd edition, New York: Wiley, 1998.

[60] E. B. Rosa, *The self and mutual inductances of linear conductors*, National Bureau of Standards, Vol. 4, (1908), 301 – 344.